AGU PUBLICATIONS

JGR

Journal of Geophysical Research: Space Physics

RESEARCH ARTICLE
10.1002/2015JA021204

Key Points:
- $d\mathbf{J}_{eq}/dt$ peaks at the premidnight and prenoon ends of the westward electrojet
- Prenoon peak is most intense when IMF is radial and solar wind speed high
- Premidnight peak develops during substorms together with substorm auroras

Correspondence to:
L. Juusola,
liisa.juusola@fmi.fi

Citation:
Juusola, L., K. Kauristie, M. van de Kamp, E. I. Tanskanen, K. Mursula, T. Asikainen, K. Andréeová, N. Partamies, H. Vanhamäki, and A. Viljanen (2015), Solar wind control of ionospheric equivalent currents and their time derivatives, *J. Geophys. Res. Space Physics*, *120*, 4971–4992, doi:10.1002/2015JA021204.

Received 10 MAR 2015
Accepted 2 MAY 2015
Accepted article online 8 MAY 2015
Published online 2 JUN 2015

Solar wind control of ionospheric equivalent currents and their time derivatives

L. Juusola[1], K. Kauristie[1], M. van de Kamp[1], E. I. Tanskanen[1], K. Mursula[2], T. Asikainen[2], K. Andréeová[1,3], N. Partamies[1,4], H. Vanhamäki[1,2], and A. Viljanen[1]

[1]Finnish Meteorological Institute, Helsinki, Finland, [2]Astronomy and Space Physics, University of Oulu, Oulu, Finland, [3]Department of Physics, University of Helsinki, Helsinki, Finland, [4]University Centre in Svalbard, Longyearbyen, Norway

Abstract A solid understanding of the solar wind control of ground magnetic field disturbances is essential for utilizing the existing long time series of ground data to obtain information on solar wind-magnetosphere-ionosphere coupling. We have used 20 years of International Monitor for Auroral Geomagnetic Effects magnetometer data (54°–76° magnetic latitude) to study the solar wind control of the ionospheric equivalent current density and its time derivative ($< |d\mathbf{J}_{eq}/dt| >$). We found that $< |d\mathbf{J}_{eq}/dt| >$ peaks at the premidnight and prenoon ends of the westward electrojet. The prenoon $< |d\mathbf{J}_{eq}/dt| >$ peak was most intense during fast solar wind and radial interplanetary magnetic field (IMF). The location of the peak was not affected by the IMF orientation but persisted at 8–10 magnetic local time and 70°–75° latitude, near the boundary between the westward and eastward electrojets. Sensitivity of this boundary to disturbances was suggested as a possible explanation for the persistent prenoon location of the peak. The premidnight peak was most intense during southward IMF orientation. While faster solar wind mainly resulted in more intense $< |d\mathbf{J}_{eq}/dt| >$ in the premidnight sector, stronger IMF caused the region of intense $< |d\mathbf{J}_{eq}/dt| >$ to spread to the postmidnight, dawn, and dusk sectors. A good correspondence was found between development of the nightside $< |d\mathbf{J}_{eq}/dt| >$ intensification and average substorm bulge and oval aurora as determined by Gjerloev et al. (2007). The bulge aurora covered the western end of the westward electrojet where the equivalent current also had a significant poleward component. The substorm oval aurora, on the other hand, extended eastward along the westward electrojet.

1. Introduction

Ground magnetic field data are available in long time series that could provide information on the driving solar wind conditions even before the start of direct solar wind observations. Such interpretations, however, require a solid understanding of the solar wind control of the ground magnetic field disturbances. Ground magnetic disturbance can also provide information on the processes associated with the transfer of solar wind energy into the magnetosphere-ionosphere system as well as the processes associated with the dissipation of that energy. An ionospheric equivalent current map is a representation of combined ground magnetic field data from several stations. In general, high-latitude ionospheric equivalent current density vectors tend to be antiparallel to $\mathbf{E} \times \mathbf{B}$ flow vectors [*Weygand et al.*, 2012]. The flow pattern, in turn, is largely controlled by the interplanetary magnetic field (IMF) and solar wind plasma [*Dungey*, 1961; *Axford and Hines*, 1961; *Dungey*, 1963; *Russell*, 1972; *Luhmann et al.*, 1984; *Weimer*, 1995, 1996; *Milan*, 2004; *Imber et al.*, 2006, 2007; *Juusola et al.*, 2014a].

Energy transfer from the solar wind into the magnetosphere is often described using coupling functions. Several functional forms exist, but the solar wind parameters typically included are two components of the IMF, B_z and B_y, and solar wind speed [e.g., *Newell et al.*, 2007, and references therein]. IMF B_x is typically not included. IMF B_x is generally not included in global self-consistent magnetohydrodynamic simulations either, as a varying nonzero IMF B_x would lead to $\nabla \cdot \mathbf{B} \neq 0$ in the solver [*Roe*, 1981].

Because geomagnetically induced currents occur together with large time derivatives of the ground magnetic field ($d\mathbf{H}/dt$) [*Viljanen*, 1997; *Boteler et al.*, 1998; *Pirjola*, 2000], characteristics of intense $d\mathbf{H}/dt$ have been extensively studied [*Viljanen et al.*, 2001, 2006; *Viljanen and Tanskanen*, 2011]. Intense $d\mathbf{H}/dt$ are typically associated with the westward electrojet [*Viljanen and Tanskanen*, 2011]. In the premidnight and midnight sectors, intense $d\mathbf{H}/dt$ are related to changes in the electrojet amplitude, while in the dawn sector, intense $d\mathbf{H}/dt$

are associated with geomagnetic pulsations [*Viljanen and Tanskanen*, 2011]. Characteristics of the weaker but more typical values, however, have received less attention.

Weigel et al. [2003] have shown that the average time derivative of the north-south component of the ground magnetic field ($|dB_x/dt|$) has two peaks, one in the prenoon sector around 9 magnetic local time (MLT) and one in the premidnight sector around 23 MLT, and that the sign changes of the average ground B_x take place approximately in the same sectors. *Weigel et al.* [2003] also showed that of the solar wind drivers, the solar wind speed has the strongest effect on the dayside $|dB_x/dt|$ peak and IMF B_z almost no effect. Thus, *Weigel et al.* [2003] attributed the driving of the dayside $|dB_x/dt|$ peak to the Kelvin-Helmholtz instability and the asymmetry about noon to the typical spiral orientation of the IMF. This indicates that different IMF orientations would then be expected to produce a peak at different dayside MLTs, but *Weigel et al.* [2003] did not examine this.

Weigel et al. [2003] also did not consider the effects of IMF B_x, although it could be an important driver of disturbances in the dayside magnetosphere and ionosphere. Especially, when B_x is the dominant IMF component, a highly turbulent foreshock forms directly upstream of the bow shock in front of Earth's magnetosphere [e.g., *Eastwood et al.*, 2005]. The foreshock is a significant source of ultralow-frequency (ULF) wave activity, which can penetrate the magnetopause and cause disturbances in the magnetosphere, ionosphere, and on the ground. High-speed solar wind is generally associated with more fluctuations than slow solar wind [*Marsch and Tu*, 1990; *Snekvik et al.*, 2013], indicating that an increased speed should enhance the effect.

It is clear that the ground magnetic field and its time derivative do not always behave similarly or have the same dependence on solar wind and IMF drivers. The response also depends on local time. Nightside $d\mathbf{H}/dt$ activity is mainly associated with the loading-unloading or substorm [*Caan et al.*, 1978] cycle driven by a southward IMF orientation and fast solar wind speed, whereas dayside $d\mathbf{H}/dt$ activity might be expected to be associated with a radial IMF orientation and fast solar wind speed. Moreover, depending on the IMF orientation, disturbance on either dayside or nightside might be more prevalent.

In this study, we have used 20 years of ground-based magnetic field measurements from the North European International Monitor for Auroral Geomagnetic Effects (IMAGE) [*Tanskanen*, 2009] from 1994 to 2013 to study the solar wind and IMF control of the ionospheric equivalent currents and their time derivatives at different magnetic latitudes and local times. We will start by introducing the data used (section 2), then show (section 3) and discuss the results (section 4), and summarize the conclusions (section 5).

2. Data and Methods

The main sources of the ground magnetic field disturbances at high latitudes are horizontal ionospheric currents between about 90 and 130 km altitude [*Kamide et al.*, 1977]. Ground magnetic measurements are often most conveniently represented in the form of equivalent currents. By definition, the ionospheric equivalent current is a spherical divergence-free sheet current that produces the same magnetic field below the ionosphere as the real ionospheric and field-aligned currents. In principle, such an equivalent current can always be uniquely defined for any ground magnetic disturbance field. At high magnetic latitudes we can approximately assume that the field-aligned currents flow radially into or out of the ionosphere, in which case the ionospheric equivalent current is equal to the divergence-free part of the real ionospheric current. For a further discussion about equivalent currents see, e.g., *Vanhamäki and Amm* [2011, and references therein].

In this study, we have used the north-south (B_x) and east-west (B_y) components of the magnetic field from the 10 s IMAGE ground magnetometer data between 1994 and 2013. Derivation of maps of the equivalent current density and its time derivative as a function of Altitude Adjusted Corrected Geomagnetic Coordinates (AACGM) latitude and magnetic local time (MLT) [*Baker and Wing*, 1989] from IMAGE data for every 10 s from 1994 to 2013 is described by *Juusola et al.* [2015]. Here we briefly summarize the procedure.

First, a baseline consisting of the regular quiet time variations in the magnetic field was subtracted from the magnetometer data using the method by *van de Kamp* [2013]. The remaining data consist of the disturbance magnetic field caused by the components of ionospheric currents which are due to space weather disturbances as well as currents induced in the solid Earth. The induced currents strengthen the horizontal disturbance magnetic field by about 10–20%, although at substorm onset the internal contribution can be up to 40% [*Tanskanen et al.*, 2001]. Thus, assuming that the internal contribution to the disturbance magnetic field is negligible may result in somewhat overestimated ionospheric equivalent current density amplitudes.

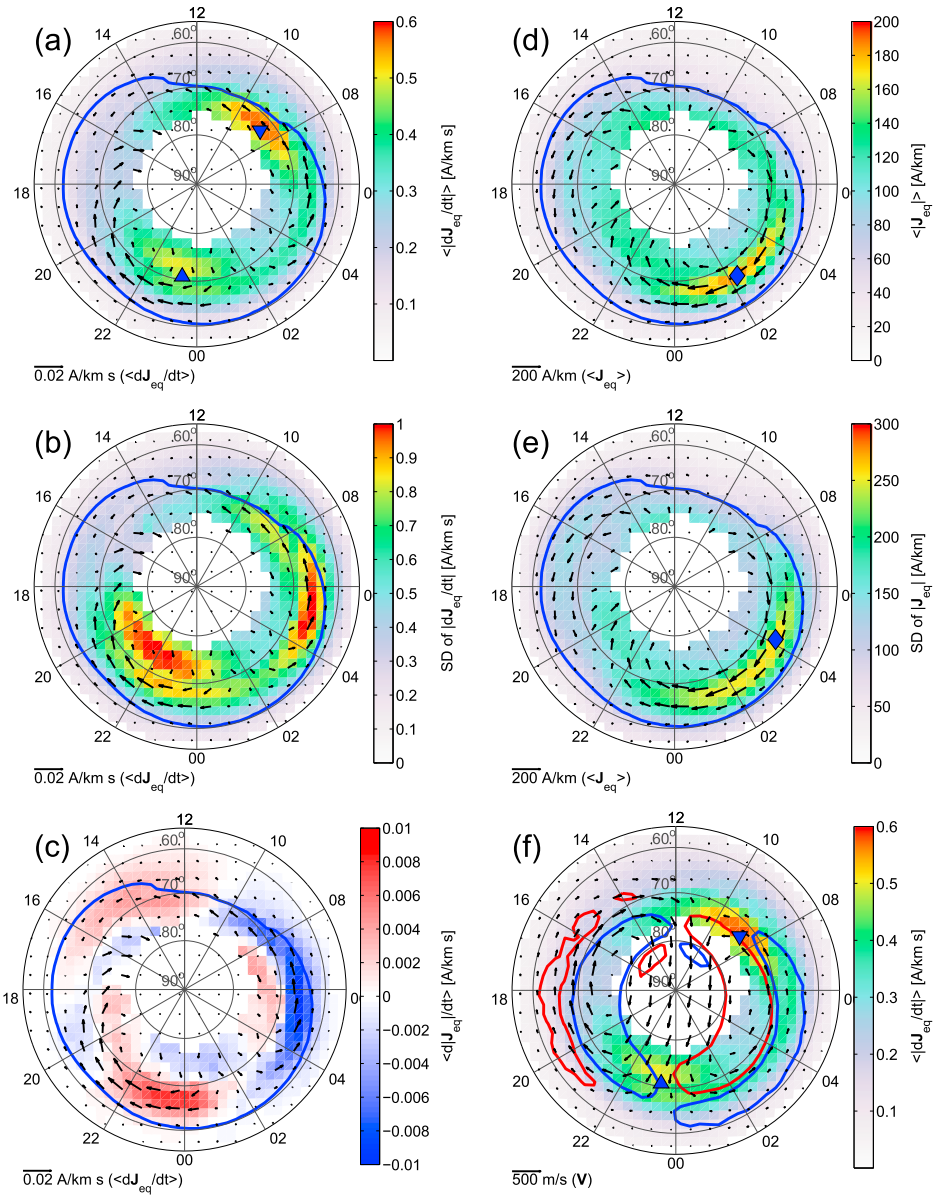

Figure 1. Averages of all data. (a) $< |d\mathbf{J}_{eq}/dt| >$ (color) and $< d\mathbf{J}_{eq}/dt >$ (arrows) for the time derivative of the equivalent current density over the 20 year interval 1994–2013 as a function of AACGM latitude and MLT. The location of the dayside maximum $< |d\mathbf{J}_{eq}/dt| >$ is marked with the blue upside down triangle and the location of the nightside maximum $< |d\mathbf{J}_{eq}/dt| >$ with the blue triangle. The blue curve is the 50 A/km contour of $< |\mathbf{J}_{eq}| >$. (b) The same as Figure 1a except that the color shows the standard deviation (SD) of $|d\mathbf{J}_{eq}/dt|$. (c) The same as Figure 1a except that the color shows $< d|\mathbf{J}_{eq}|/dt >$. (d) $< |\mathbf{J}_{eq}| >$ (color) and $< \mathbf{J}_{eq} >$ (arrows). The location of the maximum $< |\mathbf{J}_{eq}| >$ is marked with the blue diamond. The blue curve is the same as in Figure 1a. (e) The same as Figure 1d except that the color and blue diamond show the standard deviation of $|\mathbf{J}_{eq}|$ and the location of its maximum. (f) The colors and the blue triangles are the same as in Figure 1a, but the arrows show the $\mathbf{E} \times \mathbf{B}$ drift velocity ($< \mathbf{V} >$), derived from Super Dual Auroral Radar Network (SuperDARN) measurements [*Juusola et al.*, 2014a]. The blue (upward) and red (downward) curves are the ± 0.1 A/km^2 contours of the field-aligned current density ($< j_{||} >$), derived from Challenging Minisatellite Payload (CHAMP) satellite magnetic field measurements [*Juusola et al.*, 2014a].

Next, we used the 2-D Spherical Elementary Current System method [*Amm*, 1997; *Amm and Viljanen*, 1999] to derive maps of the ionospheric equivalent current density ($\mathbf{J}_{eq}(t)$ [A/km]) at 100 km altitude from the disturbance magnetic field. For the maps, we used a grid that covered the AACGM latitudes 54.0°–75.6° with steps of 0.6° and the AACGM longitudes 85.4°–116.2° with steps of 1.4°. Finally, corresponding maps of the time derivative of the equivalent current density for each epoch t were obtained by subtracting the map of the subsequent epoch (t + 10 s) from the map of the previous epoch (t − 10 s): $\mathrm{d}\mathbf{J}_{eq}/\mathrm{d}t = (\mathbf{J}_{eq}(t + 10\mathrm{s}) - \mathbf{J}_{eq}(t - 10\mathrm{s}))/20\mathrm{s}$.

Maps of the mean and standard deviation of both the equivalent current density ($\mathbf{J}_{eq}$, $|\mathbf{J}_{eq}|$) and the time derivative of the equivalent current density ($\mathrm{d}\mathbf{J}_{eq}/\mathrm{d}t$, $|\mathrm{d}\mathbf{J}_{eq}/\mathrm{d}t|$, $\mathrm{d}|\mathbf{J}_{eq}|/\mathrm{d}t$) were calculated on an AACGM latitude-MLT grid similar to that used by *Milan et al.* [2010] and *Juusola et al.* [2014a]. Examples of the resulting distributions are shown in Figure 1 (discussed in section 3.1). In Figure 1, we only show the arrows for every other grid point, for clarity.

The statistical maps were constructed from the 10 s maps. Only grid points of the 10 s maps within 200 km horizontal distance [*Juusola et al.*, 2015] from the closest operational magnetometer were included when calculating the statistical maps. The temporal mean (denoted by "< >") was calculated from the x and y components of the equivalent current density and its time derivative for each grid cell separately as

$$< \mathrm{d}\mathbf{J}_{eq}/\mathrm{d}t > = < \mathrm{d}J_{eq,x}/\mathrm{d}t > \mathbf{x} + < \mathrm{d}J_{eq,y}/\mathrm{d}t > \mathbf{y} \quad (1)$$

$$< |d\mathbf{J}_{eq}/\mathrm{d}t| > = < \sqrt{(\mathrm{d}J_{eq,x}/\mathrm{d}t)^2 + (\mathrm{d}J_{eq,y}/\mathrm{d}t)^2} > \quad (2)$$

$$< \mathrm{d}|\mathbf{J}_{eq}|/\mathrm{d}t > = < \mathrm{d}\sqrt{J_{eq,x}^2 + J_{eq,y}^2}/\mathrm{d}t > \quad (3)$$

$$< \mathbf{J}_{eq} > = < J_{eq,x} > \mathbf{x} + < J_{eq,y} > \mathbf{y} \quad (4)$$

$$< |\mathbf{J}_{eq}| > = < \sqrt{J_{eq,x}^2 + J_{eq,y}^2} > \quad (5)$$

Thus, $|< \mathrm{d}\mathbf{J}_{eq}/\mathrm{d}t >|$ (e.g., arrow length in Figure 1a) and $< |\mathrm{d}\mathbf{J}_{eq}/\mathrm{d}t| >$ (color in Figure 1a) or $|< \mathbf{J}_{eq} >|$ (arrow length in Figure 1d) and $< |\mathbf{J}_{eq}| >$ (color in Figure 1d) are not expected to be equal. Our motivation for using different definitions to describe the average behavior of the time derivative of the equivalent current density was that while $< \mathrm{d}\mathbf{J}_{eq}/\mathrm{d}t >$ (equation (1)) could be used to detect systematic preferences for certain directions, $< \mathrm{d}|\mathbf{J}_{eq}|/\mathrm{d}t >$ (equation (3)) would reveal possible increases and decreases in the equivalent current density strength. In case the directions were random but the vectors long, both $< \mathrm{d}\mathbf{J}_{eq}/\mathrm{d}t >$ and $< \mathrm{d}|\mathbf{J}_{eq}|/\mathrm{d}t >$ would be small but $< |\mathrm{d}\mathbf{J}_{eq}/\mathrm{d}t| >$ (equation (2)) large.

In order to create statistical maps for different solar wind plasma and IMF conditions, solar wind data in geocentric solar magnetospheric coordinates at 1 min resolution, propagated to the Earth's bow shock nose, were extracted from NASA/Goddard Space Flight Center's (GSFC) OMNI data set through the OMNIWeb interface (http://omniweb.gsfc.nasa.gov/). The OMNIWeb data were further delayed by 15 min in order to take into account the signal transit time from the magnetopause to the ionosphere [*Weimer et al.*, 2003].

In order to construct a statistical equivalent current density map (or a time derivative map) corresponding to a set of certain solar wind and IMF conditions, for example, southward IMF orientation with IMF amplitude $B \leq 5$ nT and x component of the solar wind speed $V_x \geq -400$ km/s, all epochs in a time series of the solar wind data from 1994 to 2013 fulfilling all the prescribed criteria were given the value "1" while all the other epochs were given the value "0." In the resulting time series of ones and zeros, any continuous intervals of zeros shorter than 15 min were removed by replacing the zeros with ones. The resulting intervals of ones could have any length (≥1 min). The statistical equivalent current density map was then constructed from all the instantaneous equivalent current density maps with their epoch corresponding to 1 using equations (1)–(5).

For the interval 1994–2013, the temporal mean values of the OMNI 1 min data for the three components and strength of the solar wind velocity and IMF were $<\mathbf{V}> = (-430, -2.4, -1.5)$ km/s, $< |\mathbf{V}| > = 430$ km/s, $< \mathbf{B} > = (0.0, 0.0, -0.1)$ nT, and $< |\mathbf{B}| > = 5.8$ nT. V_y and V_z are here given in geocentric solar ecliptic coordinates.

3. Results

3.1. Latitude and Local Time Variation

Figure 1a shows $< |d\mathbf{J}_{eq}/dt| >$ (color) and $< d\mathbf{J}_{eq}/dt >$ (arrows) for the time derivative of the equivalent current density over the 20 year interval 1994–2013 as a function of AACGM latitude and MLT. The location of the dayside maximum $< |d\mathbf{J}_{eq}/dt| >$ is marked with the blue upside down triangle and the location of the nightside maximum $< |d\mathbf{J}_{eq}/dt| >$ with the blue triangle. The blue curve is the 50 A/km contour of $< |\mathbf{J}_{eq}| >$. Figure 1b is otherwise the same as Figure 1a except that the color shows the standard deviation (SD) of $|d\mathbf{J}_{eq}/dt|$. Figure 1c is otherwise the same as Figure 1a except that the color shows $< d|\mathbf{J}_{eq}|/dt >$. Figure 1d shows $< |\mathbf{J}_{eq}| >$ (color) and $< \mathbf{J}_{eq} >$ (arrows). The location of the maximum $< |\mathbf{J}_{eq}| >$ is marked with the blue diamond. The blue curve is the same as in Figure 1a. Figure 1e is otherwise the same as Figure 1d except that the color and blue diamond show the standard deviation of $|\mathbf{J}_{eq}|$ and the location of its maximum, respectively. The colors and the blue triangles in Figure 1f are the same as in Figure 1a, but the arrows show the $\mathbf{E} \times \mathbf{B}$ drift velocity ($< \mathbf{V} >$), derived from Super Dual Auroral Radar Network (SuperDARN) measurements [*Juusola et al.*, 2014a]. The blue and red curves are the ± 0.1 A/km^2 contours of the field-aligned current density ($< j_{||} >$), derived from Challenging Minisatellite Payload (CHAMP) satellite magnetic field measurements [*Juusola et al.*, 2014a].

3.1.1. Equivalent Current Density

The equivalent current density pattern in Figure 1d shows the eastward electrojet on the duskside and the westward electrojet on the dawnside and around midnight. Only the equatorward edge of the polar cap is resolved, but the pattern suggests that in the polar cap the equivalent current is directed from the late evening sector to the prenoon sector. The blue contour indicates the region inside of which $< |\mathbf{J}_{eq}| >$ exceeds 50 A/km, which is used here as a proxy for the equatorward boundary of the auroral current system. We will call the region poleward of the curve and equatorward of the high-latitude data gap the equivalent current oval. The shape of the blue curve is not symmetrical with respect to the pole, as the most equatorward latitude ($\sim 60°$) is reached around 1 MLT and the most poleward latitude ($\sim 70°$) around 10–11 MLT. The latter is the same region where $< \mathbf{J}_{eq} >$ from the polar cap diverges to form the eastward and westward electrojets. The location is in agreement with *Viljanen and Tanskanen* [2011], who investigated the characteristics of $d\mathbf{H}/dt$ exceeding 1 nT/s at the Kilpisjärvi station (KIL, 65.88° latitude) in 1983–2010. They showed that when $d\mathbf{H}/dt$ exceeds 1 nT, $\mathbf{H}$ changes direction from southward to northward orientation around 10 MLT. They also showed that $\mathbf{H}$ changes direction from northward to southward orientation around 20 MLT, which agrees with the change from eastward to westward electrojet direction in Figure 1d.

Viljanen and Tanskanen [2011] also examined the characteristics of the total ionospheric eastward and westward equivalent current in 1994–2010 across the geographic meridian 22.1°E in the geographic latitude range of 59.0°–79.4°N. The westward current had a maximum around 2 MLT, which is where we also observe the equivalent current density maximum as well as the most southward extending equivalent current oval (Figure 1d). *Guo et al.* [2014a] reported westward electrojet current maxima between 0 MLT and 4 MLT. *Viljanen and Tanskanen* [2011] observed the peak of eastward equivalent current around 18 MLT, where we observe the most southward extending equivalent current oval of the eastward equivalent current-dominated dusk sector. *Guo et al.* [2014b] reported eastward electrojet current maxima between 16 MLT and 20 MLT. The largest standard deviation of the equivalent current density (Figure 1e) occurred in the region of the westward electrojet. The standard deviation is generally larger than the mean, which indicates that there are large variations in $|\mathbf{J}_{eq}|$.

3.1.2. Strength of the Time Derivative of the Equivalent Current Density

The color in Figure 1a shows that $< |d\mathbf{J}_{eq}/dt| >$ is elevated in two regions: in the premidnight sector and in the prenoon sector. The prenoon peak in Figure 1a is located close to the region where the equivalent current from the polar cap diverges eastward and westward (Figure 1d), with the most intense values lying on the side of the westward current. In the region of the premidnight peak, the equivalent current is westward and poleward. $< |d\mathbf{J}_{eq}/dt| >$ is also slightly enhanced within the purely westward electrojet in the postmidnight and dawn sectors. In the region of the duskside eastward electrojet, on the other hand, $< |d\mathbf{J}_{eq}/dt| >$ is low. The prenoon peak has a stronger average amplitude (maximum 0.58 A/km s) than the premidnight peak (maximum 0.50 A/km s). The premidnight peak is most likely related to substorm activity, as its shape and location agree with those of the average substorm bulge [e.g., *Gjerloev et al.*, 2007]. This will be examined further in section 3.3.

Our results agree with those of *Weigel et al.* [2003], who showed that the average ground $|dB_x/dt|$ peaks around 9 MLT and 23 MLT and that the sign changes of the average ground B_x take place approximately in the same sectors. *Viljanen and Tanskanen* [2011] showed that $d\mathbf{H}/dt$ activity at 66° latitude peaks around 0 MLT and 8 MLT and nearly vanishes at noon and early afternoon, in agreement with our Figure 1a. They also found that large $d\mathbf{H}/dt$ values occur predominantly during westward ionospheric electrojets, which we also observe.

Similar to the mean and standard deviation of $|\mathbf{J}_{eq}|$ (color in Figures 1d and 1e), the standard deviation of $|d\mathbf{J}_{eq}/dt|$ (color in Figure 1b) is generally larger than the mean (color in Figure 1a), indicating that there are large variations in $|d\mathbf{J}_{eq}/dt|$. The standard deviation of $|d\mathbf{J}_{eq}/dt|$ peaks not only in the premidnight sector but also in the dawn sector (3–7 MLT), between about 65°–70° latitude. These peaks correspond to the two regions where the most intense values of $|d\mathbf{J}_{eq}/dt|$ (top 0.0001% of the maximum $|d\mathbf{J}_{eq}/dt|$ values of the 10 s maps in 1994–2013) typically occur [*Juusola et al.*, 2015]. In the prenoon region between about 70°–75° latitude and 8–10 MLT, where the mean $< |d\mathbf{J}_{eq}/dt| >$ has its maximum, the standard deviation is only slightly enhanced (although still larger than the mean), and typically, the most intense values of $|d\mathbf{J}_{eq}/dt|$ do not occur there [*Juusola et al.*, 2015]. Thus, the more intense prenoon maximum of mean $< |d\mathbf{J}_{eq}/dt| >$ apparently consists of lower amplitude disturbances that nonetheless occur relatively frequently, whereas the less intense premidnight peak of mean $< |d\mathbf{J}_{eq}/dt| >$ includes larger values, but the disturbances do not occur as frequently as in the prenoon region. Intense disturbances also occur at dawn [*Juusola et al.*, 2015], but these are not frequent enough to produce a clear peak in the mean $< |d\mathbf{J}_{eq}/dt| >$.

3.1.3. Direction of the Time Derivative of the Equivalent Current Density

The strength of $< d\mathbf{J}_{eq}/dt >$ shown by the lengths of the arrows in Figure 1a is small (reference arrow length 0.02 A/km s) compared to $< |d\mathbf{J}_{eq}/dt| >$ (color bar scale 0.6 A/km s). Therefore, we can conclude that there are no specific regions of strongly preferred $d\mathbf{J}_{eq}/dt$ direction in the auroral oval. Instead, the tendency in the vector directions is such that on average they largely cancel each other out. This finding is consistent with the $d\mathbf{H}/dt$ direction angle analysis presented by *Viljanen and Tanskanen* [2011]. Although the $< d\mathbf{J}_{eq}/dt >$ vectors are small, they nonetheless form a distinct global pattern with relatively strong westward $< d\mathbf{J}_{eq}/dt >$ in the premidnight sector between about 60° and 70° latitude (somewhat equatorward and westward of the premidnight $< |d\mathbf{J}_{eq}/dt| >$ peak) and eastward $< d\mathbf{J}_{eq}/dt >$ in the dawn and prenoon sectors.

Figure 1c shows that for both the westward $< d\mathbf{J}_{eq}/dt >$ in the premidnight sector and the eastward $< d\mathbf{J}_{eq}/dt >$ in the prenoon sector, there is decreasing equivalent current density amplitude (blue $< d|\mathbf{J}_{eq}|/dt >$) on the western side of the region and increasing amplitude (red $< d|\mathbf{J}_{eq}|/dt >$) in the eastern side of the region. Such a pattern would be expected from magnetometers that rotate with the Earth beneath the typical equivalent current pattern: as the magnetometers travel from dusk to midnight, they would first observe weaker and weaker eastward equivalent current and then stronger and stronger westward equivalent current, producing the observed westward $< d\mathbf{J}_{eq}/dt >$. Similarly, as the magnetometers travel from dawn to noon, they would first observe weaker and weaker westward equivalent current and then stronger and stronger eastward equivalent current, producing the eastward $< d\mathbf{J}_{eq}/dt >$ observed in this sector. The weak amplitude is also in agreement with the observed $< \mathbf{J}_{eq} >$ map: at the rate of 0.02 A/km s, a change from a westward equivalent current density of 100 A/km to an eastward equivalent current density of the same amplitude (or vice versa) would occur over 2.8 h. In other words, $< d\mathbf{J}_{eq}/dt >$ and $< d|\mathbf{J}_{eq}|/dt >$ appear to correspond to spatial (east-west) derivative of the average equivalent current pattern rather than true temporal variations.

3.1.4. Relation to Field-Aligned Currents and Convection

In Figure 1f, there is downward Region 1 current on the eastern side of the premidnight region of intense $< |d\mathbf{J}_{eq}/dt| >$ and upward Region 1 current on the western side. Within this region of intense $< |d\mathbf{J}_{eq}/dt| >$, $< \mathbf{J}_{eq} >$ has a strong poleward and westward component. The equatorward mean plasma flow $< \mathbf{V} >$ from the polar cap deviates dawnward and duskward, implying that this region maps to the region in the nightside plasma sheet where fast earthward flows brake [*Shiokawa et al.*, 1997], rebound from the dipole field [*Chen and Wolf*, 1999; *Ohtani et al.*, 2009; *Panov et al.*, 2010a, 2010b; *Birn et al.*, 2011; *McPherron et al.*, 2011; *Juusola et al.*, 2013; *Nakamura et al.*, 2013], and pile up magnetic flux [*Shiokawa et al.*, 1997]. The intense $< |d\mathbf{J}_{eq}/dt| >$ extends eastward along the purely westward electrojet between the downward Region 1 current on the poleward side and upward Region 2 current on the equatorward side.

The prenoon $< |d\mathbf{J}_{eq}/dt| >$ peak is located mainly equatorward of the downward Region 1 field-aligned current, within an area of weak ($| < j_{||} > | < 0.1$ A/km^2) upward Region 2 field-aligned current. Hence, the enhancement appears to be located on closed field lines. This is in agreement with the conclusions of

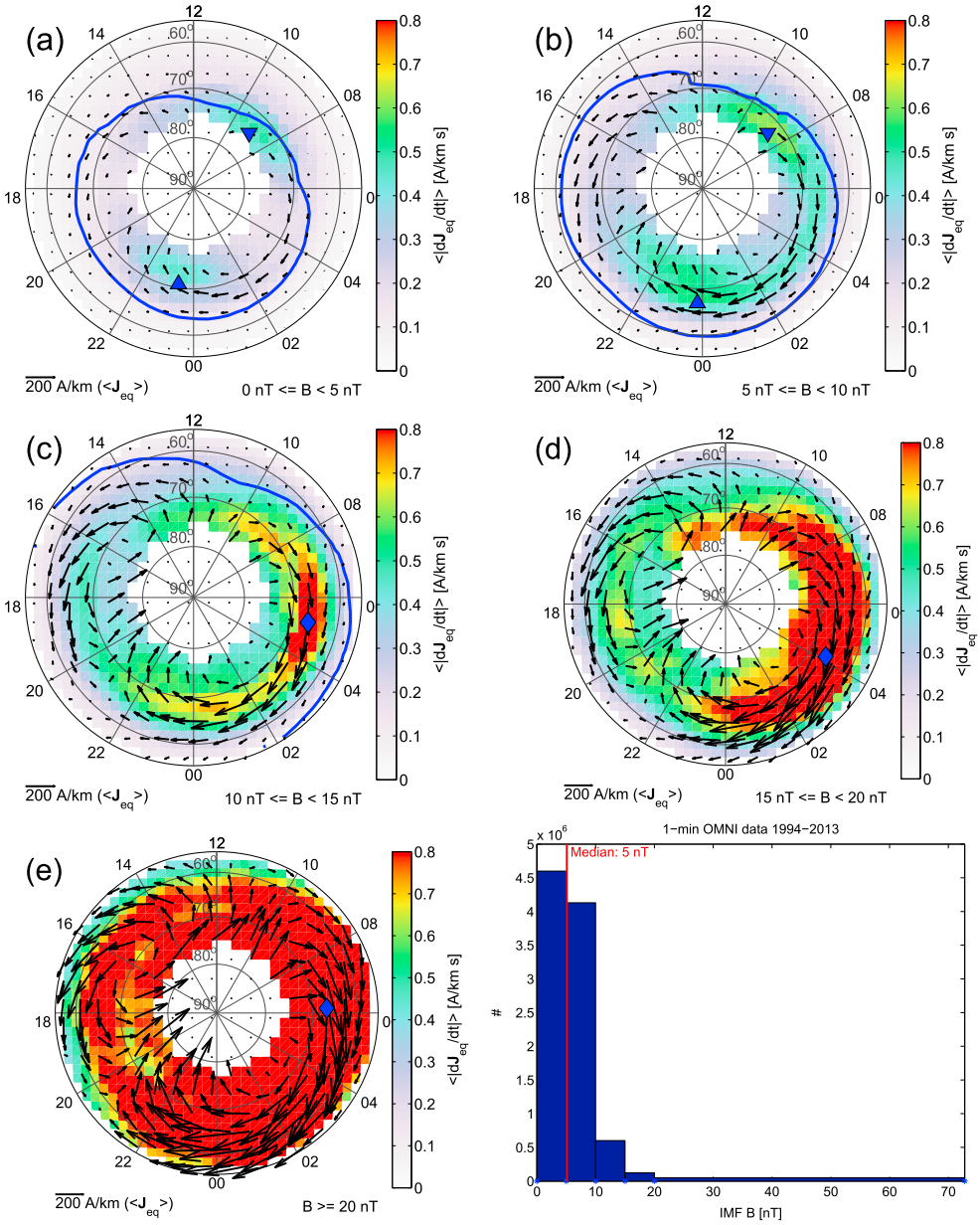

Figure 2. Dependence on IMF strength. Mean time derivative of the equivalent current density ($< |d\mathbf{J}_{eq}/dt| >$, color) and mean equivalent current density ($< \mathbf{J}_{eq} >$, arrows) as a function of AACGM latitude and MLT. If the maximum $< |d\mathbf{J}_{eq}/dt| >$ is located between 3 and 7 MLT (dawn sector), its location is shown with a blue diamond. If the maximum is not between 3 and 7 MLT, the location of the maximum between 7 and 18 MLT (dayside) is indicated with an upside down blue triangle and the location of the maximum between 18 and 3 MLT (nightside) is indicated with a blue triangle. The blue curve is the 50 A/km contour of the mean equivalent current density ($< |\mathbf{J}_{eq}| >$). The data are binned with respect to IMF strength (B). (a) 0nT $\leq B <$ 5nT, (b) 5nT $\leq B <$ 10nT, (c) 10nT $\leq B <$ 15nT, (d) 15nT $\leq B <$ 20nT, and (e) $B \geq$ 20nT. The last panel shows the number of 1 min OMNI IMF B data points in each bin.

Wing et al. [2010], according to whom field-aligned current in this latitude and MLT sector tends to be upward Region 2 that originates mainly from three possible domains: the central plasma sheet, the boundary plasma sheet, or the low-latitude boundary layer. While the first two are located on closed field lines, the low-latitude boundary layer located near the magnetopause can either be on open or closed field lines. $< \mathbf{V} >$ in the region of the prenoon $< |d\mathbf{J}_{eq}/dt| >$ peak is mainly sunward, but in the poleward section of the $< |d\mathbf{J}_{eq}/dt| >$ peak the flow direction starts to rotate antisunward. In agreement with $< \mathbf{J}_{eq} >$ (Figure 1d), the east-west component of $< \mathbf{V} >$ changes direction around 10–11 MLT.

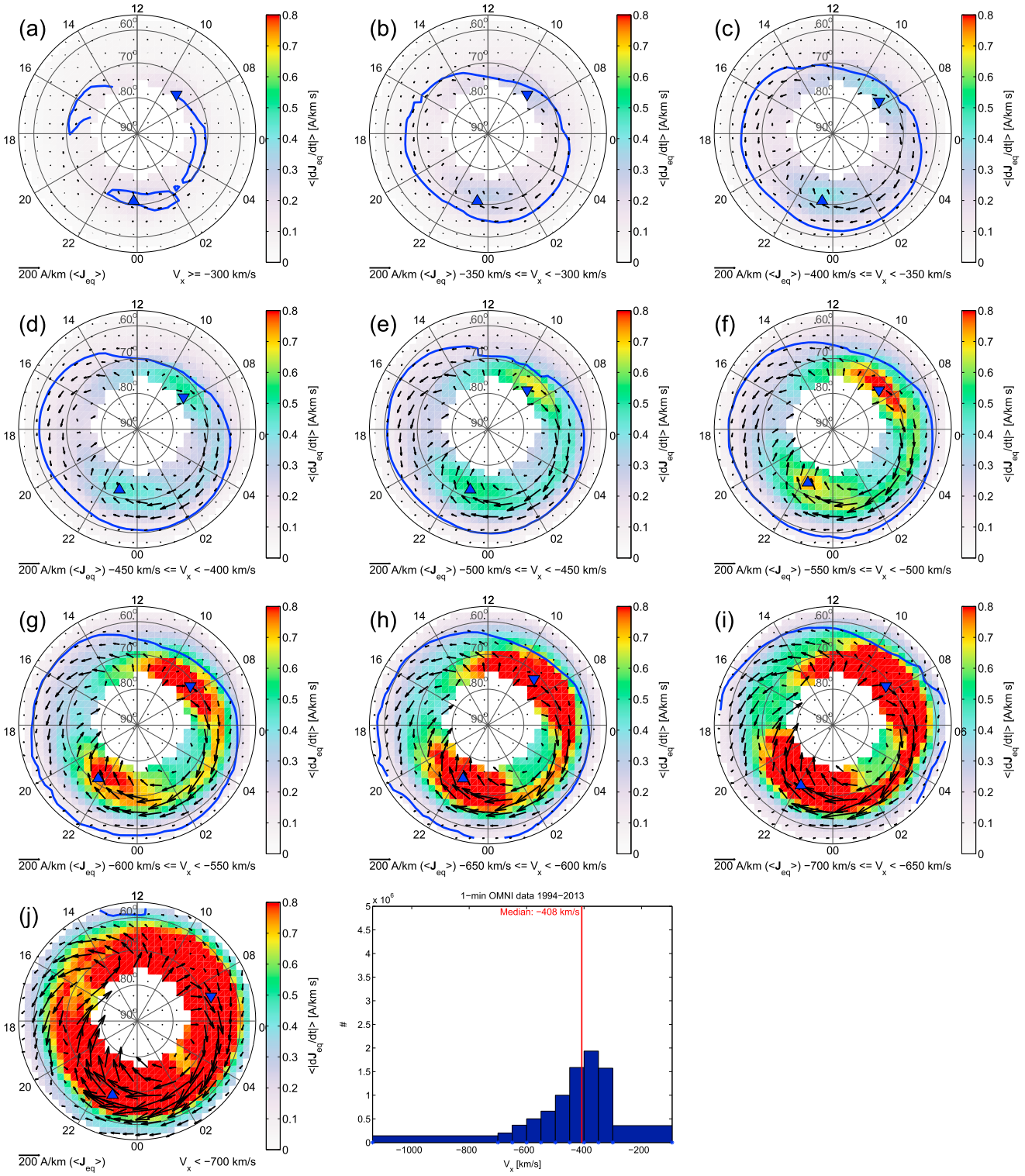

Figure 3. Dependence on solar wind speed. Mean time derivative of the equivalent current density ($< |d\mathbf{J}_{eq}/dt| >$, color) and mean equivalent current density ($< \mathbf{J}_{eq} >$, arrows) as a function of AACGM latitude and MLT. The location of the dayside maximum $< |d\mathbf{J}_{eq}/dt| >$ is marked with a blue upside down triangle and the location of the nightside maximum $< |d\mathbf{J}_{eq}/dt| >$ with a blue triangle. The blue curve is the 50 A/km contour of the mean equivalent current density ($< |\mathbf{J}_{eq}| >$). The data are binned with respect to the *x* component of the solar wind velocity (V_x). (a) $V_x \geq -300$ km/s, (b) -350 km/s $\leq V_x < -300$ km/s, (c) -400 km/s $\leq V_x < -350$ km/s, (d) -450 km/s $\leq V_x < -400$ km/s, (e) -500 km/s $\leq V_x < -450$ km/s, (f) -550 km/s $\leq V_x < -500$ km/s, (g) -600 km/s $\leq V_x < -550$ km/s, (h) -650 km/s $\leq V_x < -600$ km/s, (i) -700 km/s $\leq V_x < -650$ km/s, and (j) $V_x < -700$ km/s. The last panel shows the number of 1 min OMNI V_x data points in each bin.

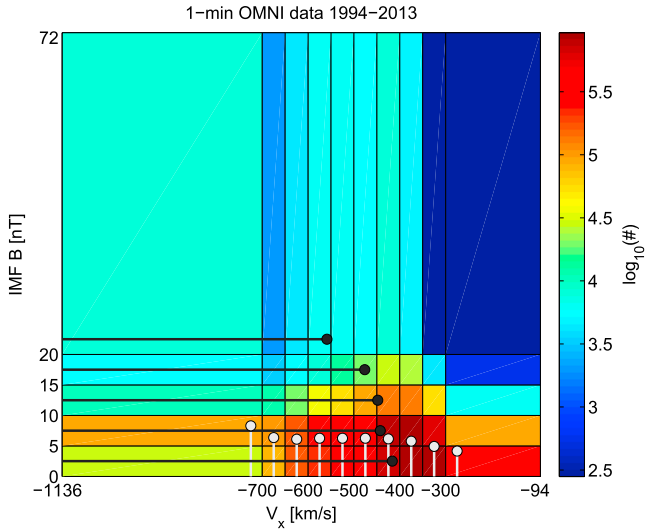

Figure 4. Number of 1 min OMNI data points in each V_x and IMF B bin (color). The white dots show the mean IMF B (smallest value 4.2 nT and largest value 8.3 nT) in each V_x bin and the black dots the mean V_x (smallest value −560 km/s and largest value −420 km/s) in each IMF B bin.

The mean (Figure 1a) and standard deviation of $|d\mathbf{J}_{eq}/dt|$ (Figure 1b) as well as the standard deviation of $|\mathbf{J}_{eq}|$ (Figure 1e) are all relatively small in the area of the duskside $<\mathbf{J}_{eq}>$ vortex (~74° latitude and ~16 MLT in Figure 1d), indicating that the vortex is a relatively stable structure. The vortex is located close to but not exactly at the same place as the $<\mathbf{V}>$ vortex (76° latitude and ~17 MLT in Figure 1f). In this area, the Region 1 field-aligned current is upward. There is a corresponding vortex on the dawnside as well (~74° latitude and ~3 MLT in Figure 1d), but this region is not as clearly a calm "eye of the storm" as the duskside vortex.

3.2. Solar Wind and IMF Control

Figure 2 shows the data binned with respect to IMF strength (B). The distributions are shown for (a) 0nT $\leq B <$ 5 nT, (b) 5 nT $\leq B <$ 10 nT, (c) 10 nT $\leq B <$ 15 nT, (d) 15 nT $\leq B <$ 20 nT, and (e) $B \geq$ 20 nT. In each panel, the color shows $<|d\mathbf{J}_{eq}/dt|>$, the arrows show $<\mathbf{J}_{eq}>$, and the blue curve is the 50 A/km contour of $<|\mathbf{J}_{eq}|>$. If the maximum $<|d\mathbf{J}_{eq}/dt|>$ is located between 3 and 7 MLT (dawn sector), its location is shown with a blue diamond. If the maximum is not between 3 and 7 MLT, the location of the maximum between 7 and 18 MLT (dayside) is indicated with the upside down blue triangle and the location of the maximum between 18 and 3 MLT (nightside) is indicated with the blue triangle. The last panel shows the number of 1 min OMNI IMF B data points in each bin. For stronger IMF, the equivalent current density increases, shifting the equatorward boundary of the equivalent current oval equatorward, and the most intense $<|d\mathbf{J}_{eq}/dt|>$ tend to concentrate in the dawn sector. The maximum $<|d\mathbf{J}_{eq}/dt|>$ values at the locations indicated by the blue triangles and diamonds are the following: Figure 2a: 0.51 A/km s (dayside) and 0.45 A/km s (nightside), Figure 2b: 0.62 A/km s (dayside) and 0.54 A/km s (nightside), Figure 2c: 0.98 A/km s (dawn), Figure 2d: 1.7 A/km s (dawn), and Figure 2e: 3.0 A/km s (dawn).

Figure 3 shows the data binned with respect to the x component of the solar wind velocity (V_x). The distributions are shown for the following: (a) $V_x \geq -300$ km/s ($<|d\mathbf{J}_{eq}/dt|>$ maxima: 0.19 A/km s (dayside) and 0.23 A/km s (nightside)), (b) -350 km/s $\leq V_x < -300$ km/s (0.29 A/km s and 0.31 A/km s), (c) -400 km/s $\leq V_x < -350$ km/s (0.40 A/km s and 0.41 A/km s), (d) -450 km/s $\leq V_x < -400$ km/s (0.52 A/km s and 0.46 A/km s), (e) -500 km/s $\leq V_x < -450$ km/s (0.68 A/km s and 0.55 A/km s), (f) -550 km/s $\leq V_x < -500$ km/s (0.82 A/km s and 0.73 A/km s), (g) -600 km/s $\leq V_x < -550$ km/s (1.1 A/km s and 0.88 A/km s), (h) -650 km/s $\leq V_x < -600$ km/s (1.3 A/km s and 1.0 A/km s), (i) -700 km/s $\leq V_x < -650$ km/s (1.6 A/km s and 1.1 A/km s), and (j) $V_x < -700$ km/s (2.1 A/km s and 1.5 A/km s). The last panel shows the number of 1 min OMNI V_x data points in each bin. For higher solar wind speed, the equivalent current density increases, shifting the equatorward boundary of the equivalent current oval equatorward. Both the prenoon and premidnight $<|d\mathbf{J}_{eq}/dt|>$ peaks intensify, but the effect is stronger in the prenoon region, such that for speeds higher than 400 km/s, the prenoon $<|d\mathbf{J}_{eq}/dt|>$ peak is more intense than the premidnight peak.

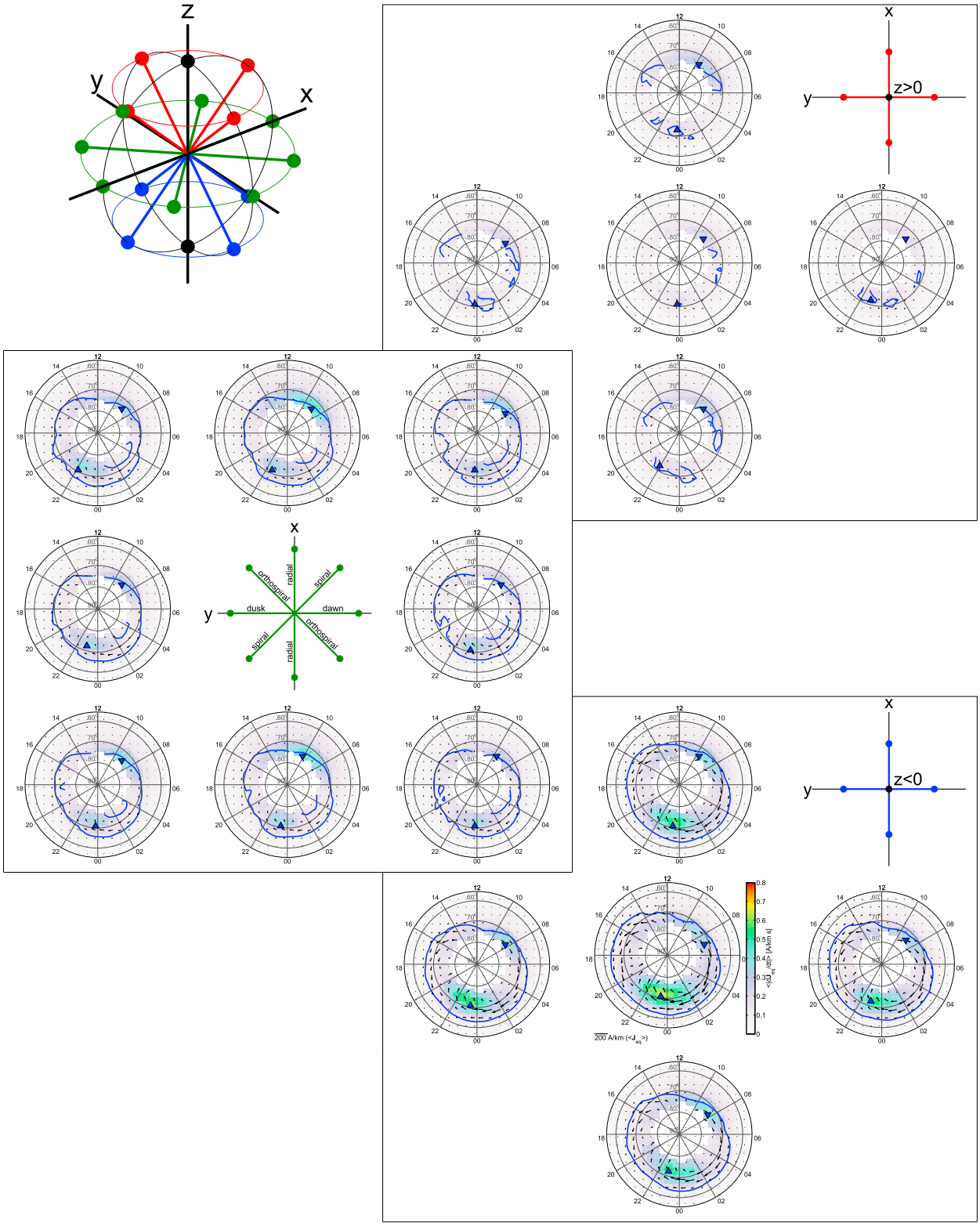

Figure 5. Dependence on IMF direction, strength, and solar wind speed. Mean time derivative of the equivalent current density (< $|d\mathbf{J}_{eq}/dt|$ >, color) and mean equivalent current density (< $\mathbf{J}_{eq}$ >, arrows) as a function of AACGM latitude and MLT. If the maximum < $|d\mathbf{J}_{eq}/dt|$ > is located between 3 and 7 MLT (dawn sector), its location is shown with a blue diamond. If the maximum is not between 3 and 7 MLT, the location of the maximum between 7 and 18 MLT (dayside) is indicated with an upside down blue triangle and the location of the maximum between 18 and 3 MLT (nightside) is indicated with a blue triangle. The blue curve is the 50 A/km contour of the mean equivalent current density (< $|\mathbf{J}_{eq}|$ >). The data are binned according to IMF direction ($B_x/B, B_y/B, B_z/B$), as graphically keyed by sets of dots at the top left and explained in the text, with the IMF amplitude $B \leq 5$ nT and x component of the solar wind velocity $V_x \geq -400$ km/s.

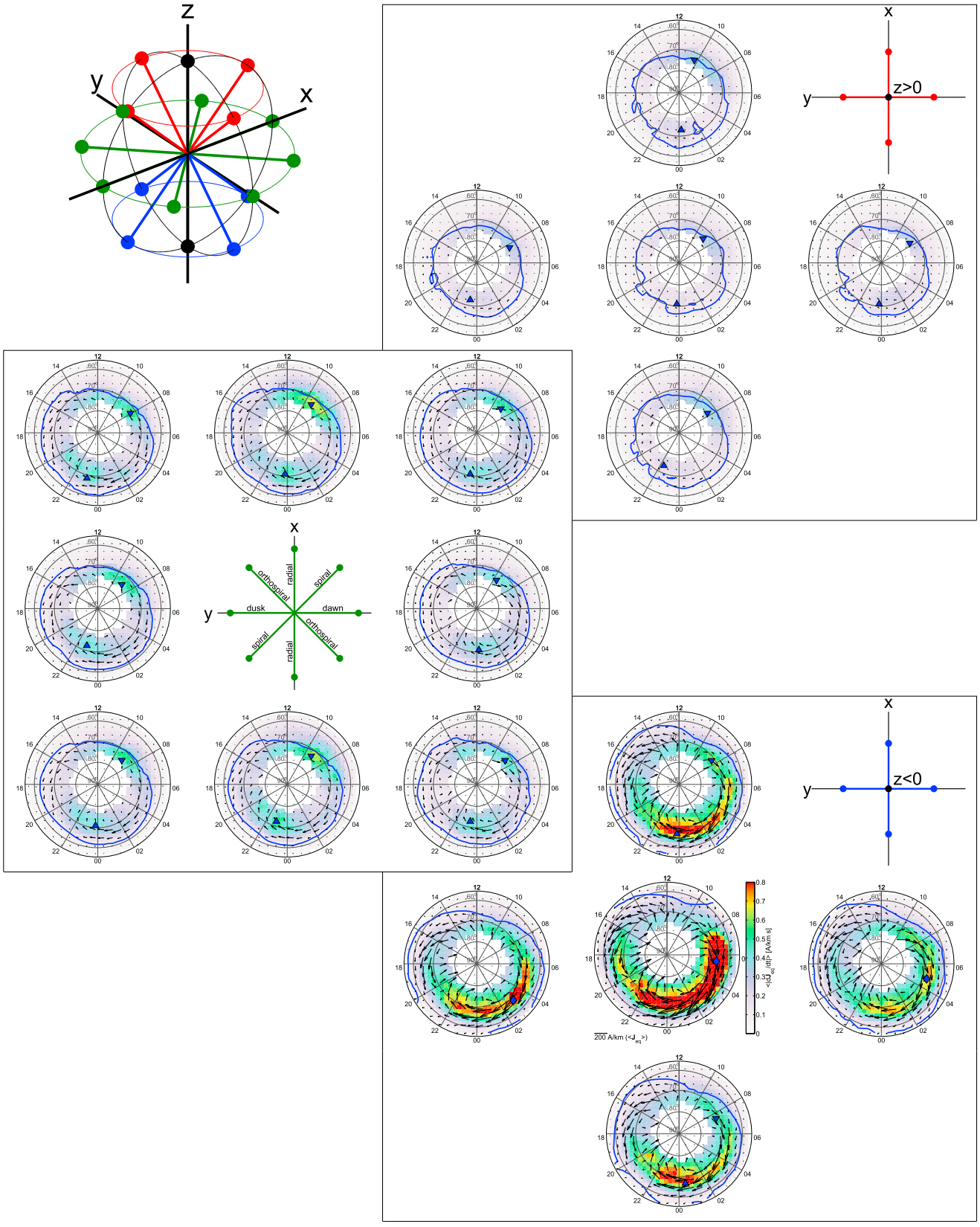

Figure 6. The same as Figure 5 except that $B > 5$ nT and $V_x \geq -400$ km/s.

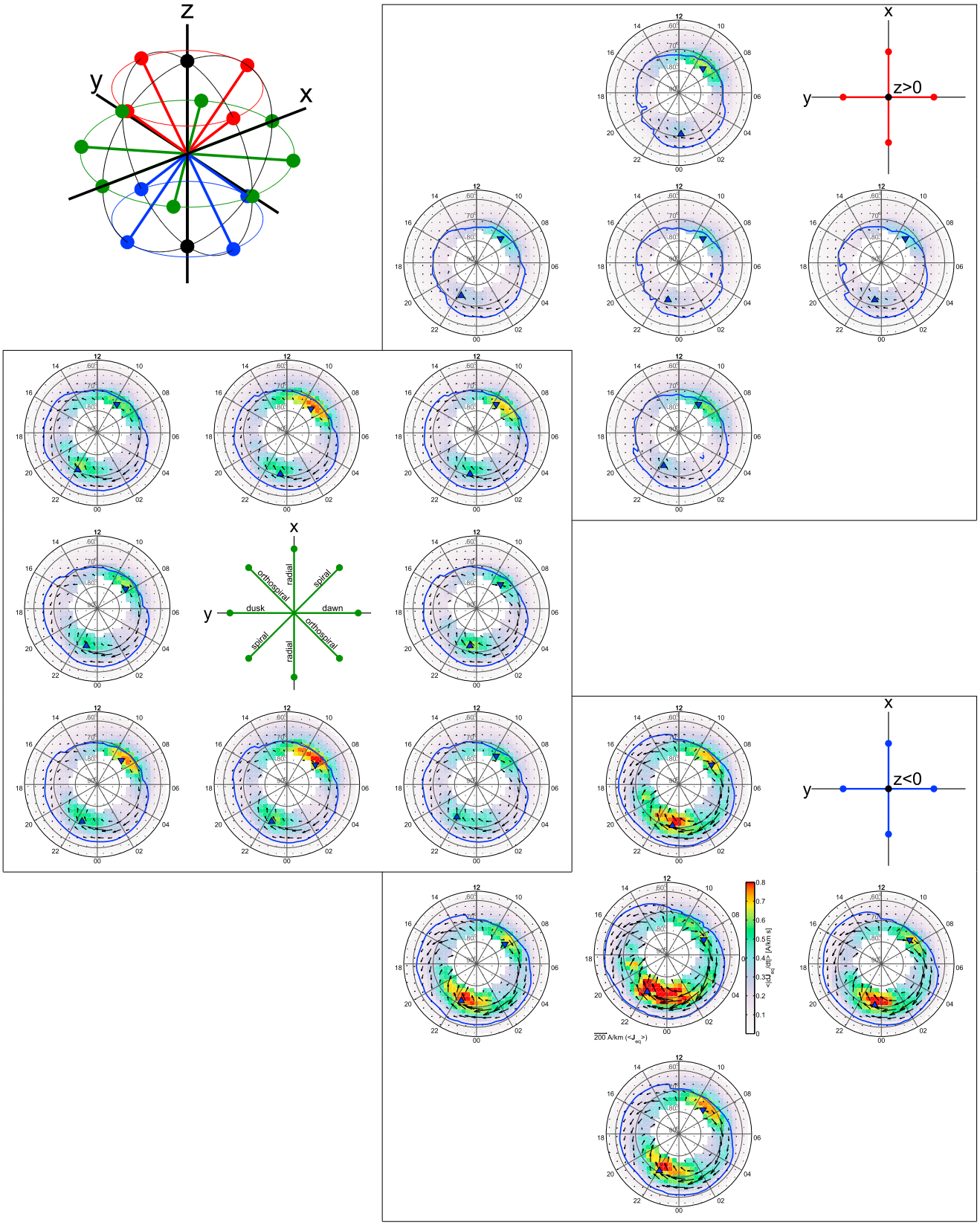

Figure 7. The same as Figure 5 except that $B \leq 5$ nT and $V_x < -400$ km/s.

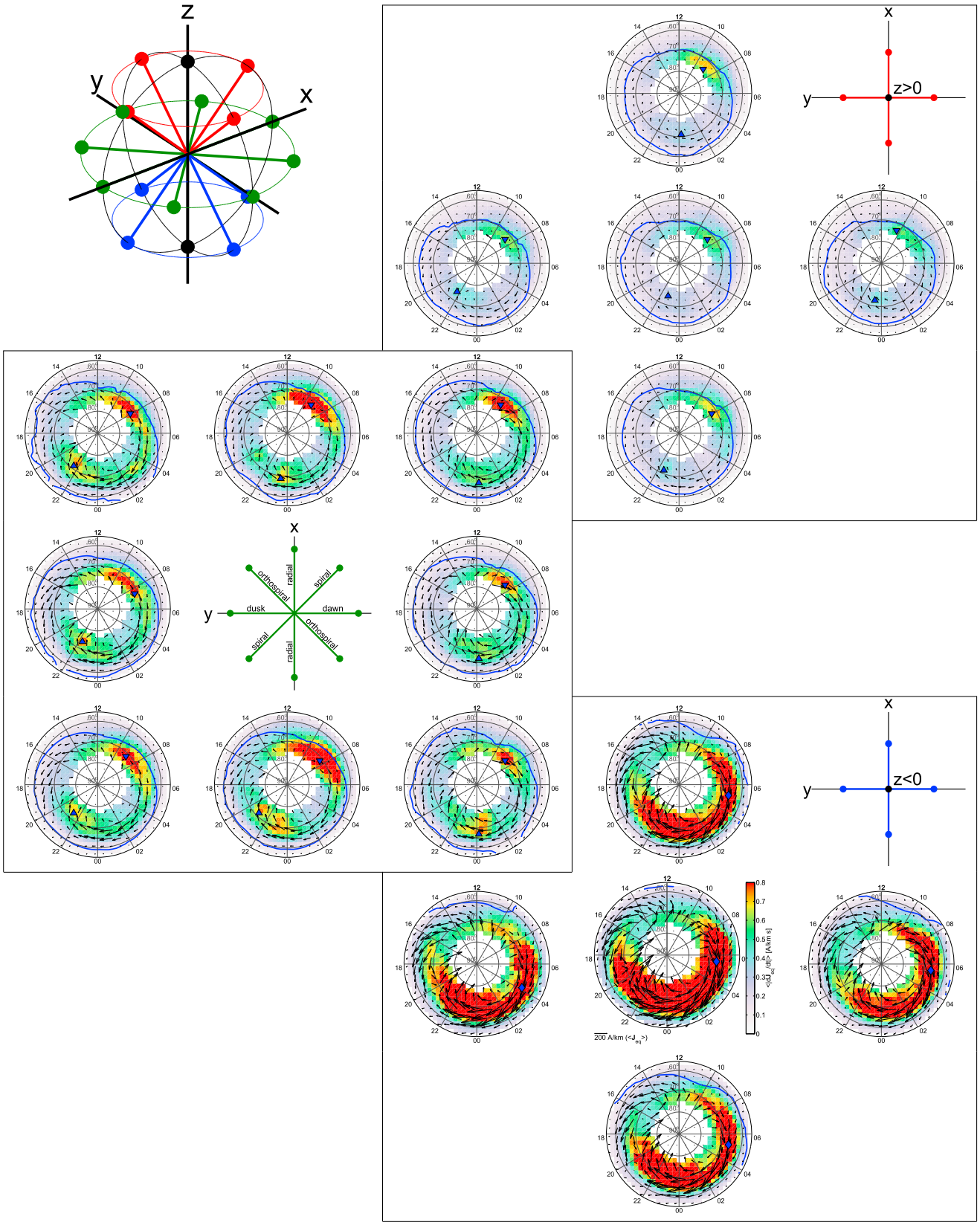

Figure 8. The same as Figure 5 except that $B > 5$ nT and $V_x < -400$ km/s.

In Figure 4, the color shows the number of 1 min OMNI data points in each V_x and IMF B bin. The white dots show the mean IMF B (smallest value 4.2 nT and largest value 8.3 nT) in each V_x bin and the black dots the mean V_x (smallest value −560 km/s and largest value −420 km/s) in each IMF B bin. When the solar wind speed increases, the IMF strength also tends to increase. Thus, the features in Figures 2 and 3 are due to combined contributions of IMF B and V_x whose properties are mutually coupled. The typical IMF orientation is also likely to change.

Figures 5–8 show $< |d\mathbf{J}_{eq}/dt| >$ (color) and $< \mathbf{J}_{eq} >$ (arrows) as a function of AACGM latitude and MLT. The data are binned according to IMF direction ($B_x/B, B_y/B, B_z/B$) in each figure but calculated for different values of B and V_x. In Figure 5, the IMF strength has been constrained to $B \leq 5$ nT and solar wind speed to $V_x \geq -400$ km/s, in Figure 6 to $B > 5$ nT and to $V_x \geq -400$ km/s, in Figure 7 to $B \leq 5$ nT and to $V_x < -400$ km/s, and in Figure 8 to $B > 5$ nT and to $V_x < -400$ km/s. IMF $B \approx 5$ nT and $V_x \approx -400$ km/s are the median values for the 20 year interval 1994–2013. The dayside and nightside or dawn maximum values of $< |d\mathbf{J}_{eq}/dt| >$, the locations of which are indicated by the blue triangles and diamonds in Figures 5–8, are listed in Table 1.

The IMF directions in the plots are illustrated by the graph in the top left corner of each figure: the black dots show the purely northward and southward IMF directions; the red dots have $B_z > 0$; the green dots have $B_z \approx 0$; and the blue dots have $B_z < 0$. The top right shows the northward IMF case (middle) and the IMF orientations corresponding to the four red dots in the top left graph (surrounding panels), organized according to B_x and B_y as indicated by the graph in the top right corner. Similarly, the bottom right shows the southward IMF case (the panel with the scales included) and the IMF orientations corresponding to the four blue dots in the top left graph. The middle left shows the IMF orientation corresponding to the green dots in the top left graph, organized according to the graph in the middle. Each plot includes those data where the IMF vector is within ±22.5° around the nominal IMF direction indicated in the graph.

IMF direction, solar wind speed, and IMF strength all affect the intensity of the prenoon $< |d\mathbf{J}_{eq}/dt| >$ peak. For all Figures 5–8, the most intense prenoon peak occurs for radial IMF orientation ($B_y \approx 0$ and $B_z \approx 0$). The second most favorable IMF orientation appears to be the spiral ($B_x \cdot B_y < 0$ and $B_z \approx 0$), at least when IMF $B \leq 5$ nT (Figures 5 and 7 and Table 1), whereas the intensity of the prenoon peak is clearly weaker for the orthospiral ($B_x \cdot B_y > 0$ and $B_z \approx 0$), dawn-dusk ($B_x \approx 0$ and $B_z \approx 0$), or $B_z \neq 0$ orientations.

For a given IMF direction, the prenoon peak is somewhat more intense for stronger IMF (Figure 6) than weaker IMF (Figure 5) and clearly more intense for faster solar wind speed (Figure 7) than for slower solar wind speed (Figure 5). Therefore, the most intense prenoon peak then occurs for a strong IMF, fast solar wind speed (Figure 8), and radial IMF orientation (Table 1).

Although the area of the prenoon peak becomes somewhat larger for faster solar wind speed, stronger IMF, and radial IMF direction, the location of its maximum does not show any significant dependence on the solar wind speed, IMF strength, or direction but remains typically between about 70°–75° latitude and 8–10 MLT. Neither does the location change with respect to the $< \mathbf{J}_{eq} >$ pattern, but the peak remains near the dayside end of the westward electrojet.

IMF direction, strength, and solar wind speed all affect the nightside $< |d\mathbf{J}_{eq}/dt| >$ activity as well, except that the most intense values (Table 1) and wide-spread activity occur for southward IMF orientation. Association of a southward IMF component with ground disturbances and a northward IMF component with quiet conditions is well known [e.g., *Fairfield and Cahill*, 1966], and *Tanskanen et al.* [2011], for example, have reported on the effect of solar wind high-speed streams on the intensity of geomagnetic activity. The IMF strength (Figure 6) has a pronounced effect over a wider MLT range than the solar wind speed (Figure 7). Especially, extension of intense $< |d\mathbf{J}_{eq}/dt| >$ to the dawn sector around 6 MLT and to the dusk sector around 18 MLT requires a strong, southward oriented IMF. In some such cases, the maximum of the nightside peak (blue triangles in Figures 5–8) even moves from the premidnight sector to the dawn sector (blue diamonds in Figures 6 and 8). For increased solar wind speed but weak IMF, the $< |d\mathbf{J}_{eq}/dt| >$ activity intensifies but tends to remain confined to the premidnight sector and around midnight.

IMF orientation seems to be the most important factor for determining the relative intensities of the prenoon and nightside $< |d\mathbf{J}_{eq}/dt| >$ peaks. Whenever IMF $B_z < 0$, the nightside peak intensifies so that it becomes stronger than the dayside peak (Table 1). Mostly, when IMF $B_z > 0$, the nightside peak weakens so that it becomes weaker than the dayside peak. For radial and spiral IMF orientations (IMF $B_z \approx 0$), the prenoon peak is in all considered cases stronger than the premidnight peak.

Table 1. Maximum $< |d\mathbf{J}_{eq}/dt| >$ in Figures 5–8[a]

		$B \leq 5$ nT $V_x \geq -400$ km/s (A/km s)	$B > 5$ nT $V_x \geq -400$ km/s (A/km s)	$B \leq 5$ nT $V_x < -400$ km/s (A/km s)	$B > 5$ nT $V_x < -400$ km/s (A/km s)
North	($B_z > 0$)	**0.28** 0.21	**0.34** 0.21	**0.48** 0.35	**0.62** 0.32
Dawn	($B_z > 0$)	0.21 0.21	**0.30** 0.27	**0.44** 0.35	**0.59** 0.43
Radial	($B_z > 0$)	**0.33** 0.23	**0.39** 0.25	**0.65** 0.37	**0.72** 0.37
Dusk	($B_z > 0$)	**0.25** 0.22	**0.36** 0.26	**0.51** 0.34	**0.62** 0.46
Radial	($B_z > 0$)	**0.32** 0.21	**0.39** 0.27	**0.60** 0.40	**0.73** 0.45
Orthospiral	($B_z \approx 0$)	0.31 **0.38**	**0.49** 0.47	**0.59** 0.52	**0.89** 0.77
Dawn	($B_z \approx 0$)	0.29 **0.37**	**0.46** 0.42	0.59 **0.63**	**0.81** 0.63
Spiral	($B_z \approx 0$)	**0.39** 0.35	**0.51** 0.42	**0.71** 0.52	**0.92** 0.62
Radial	($B_z \approx 0$)	**0.50** 0.38	**0.68** 0.49	**0.78** 0.55	**1.1** 0.73
Orthospiral	($B_z \approx 0$)	0.37 **0.42**	**0.59** 0.46	0.61 **0.63**	**0.93** 0.77
Dusk	($B_z \approx 0$)	0.33 **0.37**	**0.54** 0.46	**0.63** 0.54	**0.83** 0.77
Spiral	($B_z \approx 0$)	**0.43** 0.36	**0.54** 0.43	**0.76** 0.56	**0.94** 0.69
Radial	($B_z \approx 0$)	**0.47** 0.39	**0.63** 0.55	**0.82** 0.62	**1.1** 0.76
Dawn	($B_z < 0$)	0.36 **0.56**	0.76	0.70 **0.87**	1.3
Radial	($B_z < 0$)	0.41 **0.59**	0.63 **0.87**	0.72 **0.86**	1.3
Dusk	($B_z < 0$)	0.40 **0.59**	0.90	0.69 **0.86**	1.4
Radial	($B_z < 0$)	0.42 **0.53**	0.55 **0.84**	0.76 **0.92**	1.3
South	($B_z < 0$)	0.36 **0.66**	1.7	0.64 **0.97**	2.2

[a]Either nightside maximum (blue triangles in Figures 5–8) and dayside maximum (upside down blue triangles in Figures 5–8) or dawn maximum (blue diamonds in Figures 6 and 8) are given. In case of nightside and dayside maxima, the larger value is highlighted in bold.

The equatorward boundary of the equivalent current oval (blue curve) is also located at the most equatorward latitudes for southward IMF. However, for all IMF orientations, increasing either solar wind speed or IMF strength will move the boundary southward. The effect of IMF strength is more significant, as the ovals are larger (especially wider in latitude) in Figure 6 than in Figure 7. This is in agreement with *Finch et al.* [2008] and *Lockwood et al.* [2013a, 2013b, 2014a, 2014b]. IMF B_y affects most clearly the dayside configuration of $< \mathbf{J}_{eq} >$, as expected [e.g., *Weimer*, 1995, 1996].

According to *Weigel et al.* [2003], around 10 MLT, the most important solar wind driver for $|dB_x/dt|$ is solar wind speed, while IMF B_z has very little effect. In agreement, we observed that the prenoon $< |d\mathbf{J}_{eq}/dt| >$ peak is more intense during higher solar wind speed. *Weigel et al.* [2003] did not examine the effect of IMF B_x, but we found the radial IMF orientation to produce the most intense prenoon $< |d\mathbf{J}_{eq}/dt| >$ peak. Our observations that on the nightside a higher solar wind speed mainly produces more intense activity in the premidnight sector while a southward IMF orientation and larger IMF B together produce more intense activity also in the postmidnight sector are also in agreement with *Weigel et al.* [2003].

3.3. Substorm Development

We have compared the development of the statistical equivalent current density and its time derivative to that of substorm auroras by *Gjerloev et al.* [2007]. *Gjerloev et al.* [2007] used global auroral images at ultraviolet wavelengths during 116 substorms to obtain a statistical description of the bulge-type auroral substorm [*Akasofu*, 1964].

Gjerloev et al. [2007] described the substorm aurora as two distinct entities: the bulge aurora and the oval aurora. They give average locations for the west end of the bulge (P1), the east end of the bulge (P2), the west end of the oval aurora (P3), the east end of the oval aurora (P4), the poleward boundary of the bulge at the MLT of onset (P5), and the equatorward boundary of the auroral oval at the MLT of onset (P6) for the normalized substorm epochs $T = 0.0$ (onset), $T = 0.5$ (expansion phase), $T = 1.0$ (peak), $T = 1.5$ (recovery phase), and $T = 2.0$ (recovery phase). Normalized substorm time, where the time from onset to maximum expansion is

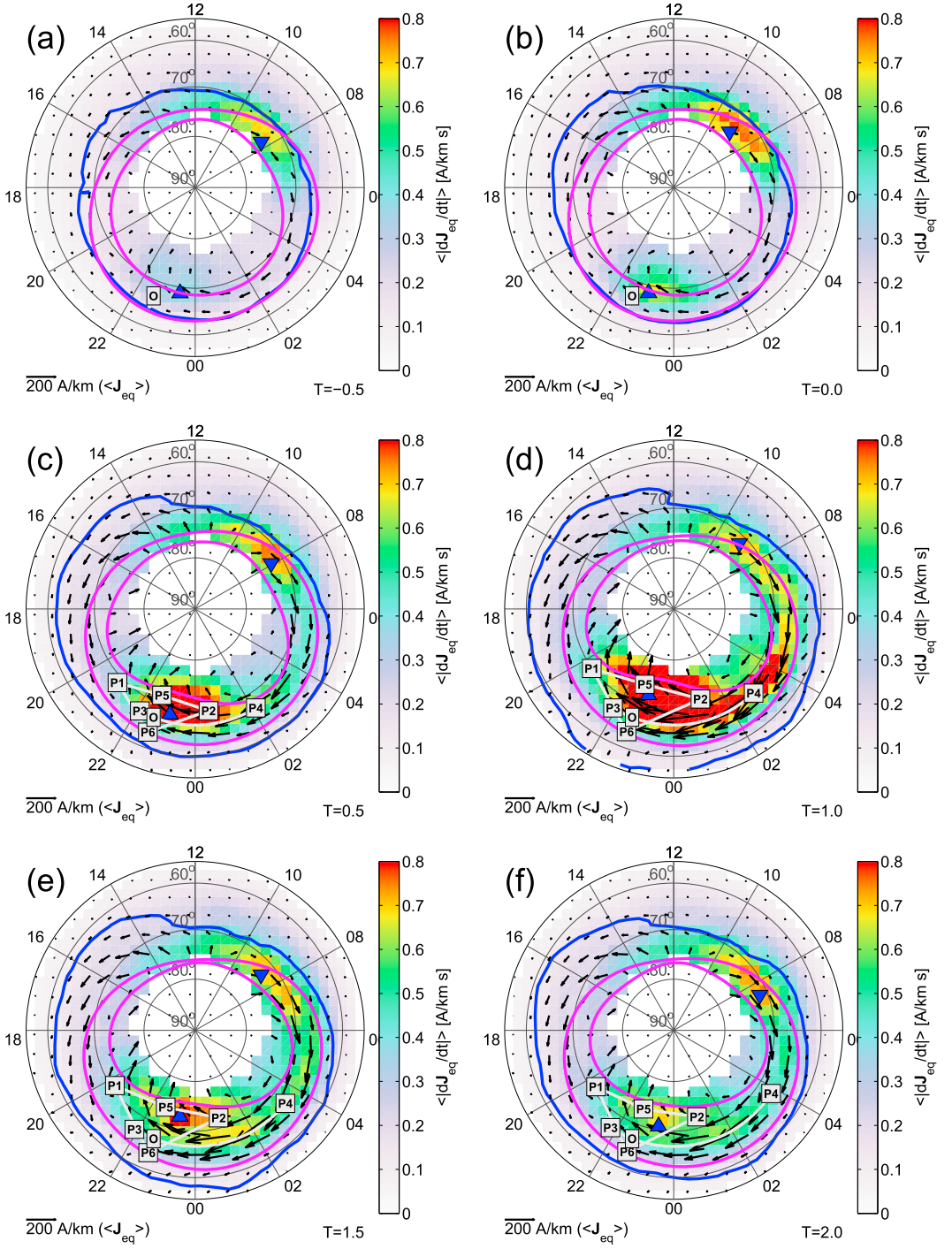

Figure 9. Substorm development. Mean time derivative of the equivalent current density ($< |d\mathbf{J}_{eq}/dt| >$, color) and mean equivalent current density ($< \mathbf{J}_{eq} >$, arrows) as a function of AACGM latitude and MLT. The location of the dayside maximum $< |d\mathbf{J}_{eq}/dt| >$ is marked with a blue upside down triangle and the location of the nightside maximum $< |d\mathbf{J}_{eq}/dt| >$ with a blue triangle. The blue curve is the 50 A/km contour of the mean equivalent current density ($< |\mathbf{J}_{eq}| >$). The data are binned according to normalized substorm time T [*Gjerloev et al.*, 2007]. (a) $T = -0.5$, growth phase. (b) $T = 0.0$, onset. (c) $T = 0.5$, expansion phase. (d) $T = 1.0$, peak. (e) $T = 1.5$, recovery phase. (f) $T = 2.0$, recovery phase. The white square labeled O indicates the average substorm onset location (occurrence at $T = 0.0$ but indicated in all panels for reference), and the white curves and squares labeled P indicate the development of an average substorm bulge ($0.0 < T \leq 2.0$; P1–P2 and P5–P6) and oval aurora (P3–P4) as determined from global auroral images at ultraviolet wavelengths [*Gjerloev et al.*, 2007]. The magenta curves show averaged auroral emission patterns for the substorm time steps according to *Gjerloev et al.* [2008].

normalized to one, was used by *Gjerloev et al.* [2007] so that the expansion phase data would not be mixed with recovery phase data.

Gjerloev et al. [2007] determined the onset and peak purely from images but showed that, on average, the *AL* index also minimizes at $T = 1$. Prior to $T = 0$, the *AL* or *AU* indices did not show any signs of a growth phase. *Gjerloev et al.* [2007] also showed that the average substorm had an *AL* minimum of −420 nT. After the minimum, there was a linear recovery such that by $T = 2$, *AL* had recovered to 40% of the minimum value. After that, *Gjerloev et al.* [2007] observed a slower recovery that lasted at least until $T = 6$.

We have used the *AL* index to identify substorm expansion phases. Because of the large amount of data, the identification was carried out using an automated algorithm [*Juusola et al.*, 2011; *Partamies et al.*, 2013]. The algorithm found altogether 74,080 expansion phases during 1994–2013. In this analysis, we have only included expansion phases not immediately preceded by a recovery phase (isolated substorm or the first cycle from a chain of multiple substorms). The number of such expansion phases was 29,526. Deleting expansion phases for which any part of the interval $-0.50 - 0.25 \leq T \leq 2.00 + 0.25$ overlapped with another expansion phase reduced the number further to 28,315.

Figure 9 shows $< |d\mathbf{J}_{eq}/dt| >$ (color) and $< \mathbf{J}_{eq} >$ (arrows) as a function of AACGM latitude and MLT for the phases of a substorm. The data are binned according to the normalized substorm time T as follows: (a) $T = -0.5 \pm 0.25$, before onset (growth phase); (b) $T = 0.0 \pm 0.25$, onset; (c) $T = 0.5 \pm 0.25$, expansion phase; (d) $T = 1.0 \pm 0.25$, peak; (e) $T = 1.5 \pm 0.25$, after expansion (recovery phase); and (f) $T = 2.0 \pm 0.25$, after expansion (recovery phase). The white square labeled "O" indicates the average substorm onset location (occurrence at $T = 0.0$ but indicated in all panels for reference), and the white curves and white squares labeled "P" indicate the development of an average substorm bulge ($0.0 < T \leq 2.0$; P1–P2 and P5–P6) and oval aurora (P3-P4) according to *Gjerloev et al.* [2007]. The white lines connecting P1, P5, P2, and P6 roughly indicate the outlines of the bulge, and the white curve connecting P3 and P4 indicates the oval aurora. Averaged auroral emission patterns for the substorm time steps derived by *Gjerloev et al.* [2008] are indicated with the magenta curves. *Gjerloev et al.* [2008] utilized the same data set of global auroral images during the 116 winter substorms as *Gjerloev et al.* [2007]. Our data set, on the other hand, includes substorms from all seasons.

Figure 9 shows that the prenoon $< |d\mathbf{J}_{eq}/dt| >$ maximum (Figure 9a: 0.70 A/km s, Figure 9b: 0.78 A/km s, Figure 9c: 0.76 A/km s, Figure 9d: 0.72 A/km s, Figure 9e: 0.73 A/km s, and Figure 9f: 0.75 A/km s) remained more or less unchanged throughout the substorm, confirming that it was not a significantly substorm-related phenomenon. The premidnight $< |d\mathbf{J}_{eq}/dt| >$ peak (Figure 9a: 0.39 A/km s, Figure 9b: 0.68 A/km s, Figure 9c: 0.98 A/km s, Figure 9d: 1.23 A/km s, Figure 9e: 0.84 A/km s, and Figure 9f: 0.70 A/km s), on the other hand, clearly was associated with substorm expansion. In general, there appears to be a good agreement between the development of the substorm aurora and intense nightside $< |d\mathbf{J}_{eq}/dt| >$ in the figure.

During the growth phase (Figure 9a), the premidnight $< |d\mathbf{J}_{eq}/dt| >$ peak was very weak. The onset took place at the equatorward edge of the westward electrojet, at its westward end. At onset (Figure 9b), the westward equivalent current poleward and westward of the onset location increased. The west end of the bulge (P1), the west end of the oval aurora (P3), and the equatorward boundary of the auroral oval (P6) appear to be associated with the western edge of the westward electrojet: the west end of the bulge (P1) expanded poleward and westward along the boundary between the eastward and westward equivalent current, the west end of the oval aurora (P3) expanded westward at the onset latitude together with the westward electrojet at this latitude, and the equatorward boundary of the auroral oval (P6) expanded equatorward at the onset MLT with the westward electrojet at this MLT. The east end of the oval aurora (P4) expanded eastward along the westward electrojet associated with an enhancement of $< |d\mathbf{J}_{eq}/dt| >$. At the end of the expansion phase (Figure 9d) and at the beginning of the recovery phase (Figure 9e), the most intense nightside $< |d\mathbf{J}_{eq}/dt| >$ (blue triangle) occurred near the poleward boundary of the bulge (P5). Throughout expansion and recovery (Figures 9c–9f), the east end of the bulge (P2) was located at the poleward boundary of the westward electrojet, at the western boundary between the purely westward equivalent current and equivalent current with a strong poleward component.

The equatorward boundary of the equivalent current oval (blue curve in Figure 9) shifted equatorward from substorm onset (Figure 9b) to substorm peak (Figure 9d), after which it started to shift poleward again. In the growth phase, at onset, and in the expansion phase, the most equatorward location of the boundary occurred around midnight. At substorm peak, the most equatorward location occurred in the premidnight sector and

in the substorm recovery phase in the postmidnight sector. According to Figure 1, postmidnight sector is where the most equatorward location of the boundary typically was located.

During the substorm growth phase (Figure 9a) and onset (Figure 9b), there was a good agreement between the equatorward boundary of the equivalent current oval (blue curve) the equatorward boundary of the average auroral emission pattern (equatorward magenta curve) around midnight and on the dawnside. The westward electrojet flowed along the auroral oval (region between the two magenta curves). Around midnight, poleward of the auroral oval the equivalent current was directed poleward. During the substorm expansion and recovery phases (Figures 9c–9f), the majority of the westward electrojet was still concentrated on the auroral oval. On the duskside, the auroral oval coincided with the boundary between the eastward electrojet and westward equivalent current in the polar cap.

To summarize, there appears to be a good correspondence between the average substorm auroras, as determined by *Gjerloev et al.* [2007], and intensified nightside $< |d\mathbf{J}_{eq}/dt| >$. The bulge aurora covered the western end of the westward electrojet where the equivalent current had a significant poleward component. The oval aurora, on the other hand, extended eastward along the purely westward electrojet.

4. Discussion

We observed that the prenoon $< |d\mathbf{J}_{eq}/dt| >$ peak was most intense for fast solar wind speed, strong IMF, and radial IMF orientation. It was more intense for spiral IMF orientation than for dawn-dusk, orthospiral or $B_z \neq 0$ IMF orientations. These results suggest that the source of the $< |d\mathbf{J}_{eq}/dt| >$ disturbances might be associated with the foreshock and quasi-parallel region of the bow shock [e.g., *Anderson*, 1994]. However, it is not clear why the $< |d\mathbf{J}_{eq}/dt| >$ peak then remained persistently in the prenoon sector. Because both the foreshock and the quasi-parallel bow shock are located upstream of the prenoon bow shock during spiral IMF orientation, and upstream of the postnoon bow shock during the rarer periods of orthospiral IMF orientation, a preference for prenoon ionospheric disturbances would be expected during spiral IMF orientation and a preference for postnoon ionospheric disturbances during orthospiral IMF orientation. During radial IMF, both the foreshock and quasi-parallel shock are located directly in front of the subsolar bow shock, and ionospheric disturbances would be expected around noon. *Andréeová et al.* [2014] showed that when the IMF is radial, ULF wave activity, caused by the foreshock, can be observed along most of the dayside geostationary orbit. During dawn-dusk or north-south IMF orientations, no foreshock or quasi-parallel bow shock would be expected, only a quasi-perpendicular bow shock, which is generally not considered to be a significant source of fluctuations.

Weigel et al. [2003] attributed the asymmetry of the dayside ground dB_x/dt peak about noon to typical IMF configurations which make the Kelvin-Helmholtz instability more likely to occur on field lines that map to the prenoon sector. Our observation that the MLT location of the prenoon $< |d\mathbf{J}_{eq}/dt| >$ peak is not affected by the IMF orientation does not agree with this interpretation.

The location of the dayside $< |d\mathbf{J}_{eq}/dt| >$ peak in the prenoon sector might simply be related to dynamics at the boundary between the westward and eastward equivalent currents. This region may be sensitive to disturbances occurring under certain driving conditions (fast solar wind speed and radial IMF configuration). Small rotations of the equivalent current pattern would cause first one electrojet and then the other to dominate. This interpretation is supported by the study of *Viljanen and Tanskanen* [2011], who showed that between 7 and 13 MLT, intense $d\mathbf{H}/dt$ is mainly southward or northward directed, which would correspond to westward and eastward $d\mathbf{J}_{eq}/dt$. The clockwise rotation of the average ionospheric two-cell convection pattern by approximately 16° about the magnetic pole is due to the auroral band of enhanced Hall conductance [e.g., *Lotko et al.*, 2014, and references therein]. Both the $\mathbf{E} \times \mathbf{B}$ drift and $< \mathbf{J}_{eq} >$ in our Figure 1 show this rotation, as does $< \mathbf{J}_{eq} >$ for different IMF directions in Figures 5–8. What is not clear is why the prenoon $< |d\mathbf{J}_{eq}/dt| >$ peak is not located at the point where $< \mathbf{J}_{eq} >$ changes direction but is shifted toward the westward $< \mathbf{J}_{eq} >$. Figure 9 may show a possible explanation: two main regions where equivalent current leaves and enters the auroral oval coincide with the premidnight and prenoon $< |d\mathbf{J}_{eq}/dt| >$ peaks, respectively.

The prenoon location of the $< |d\mathbf{J}_{eq}/dt| >$ peak also agrees with the reported occurrence of traveling convection vortices (TCVs) [*Lanzerotti et al.*, 1991]. TCVs that move antisunward from noon at high latitudes (~75°) cause magnetic disturbances of about 100 nT peak amplitude. According to *Lanzerotti et al.* [1991], when the IMF orientation is not considered, the majority of TCVs is concentrated between about 5 and 15 local time (LT), with a clear occurrence peak at 8–10 LT and minimum at 11 LT. *Korotova et al.* [2004], however, observed

dawnward moving disturbances in ground and geosynchronous magnetometer observations prior to noon during spiral IMF orientation and duskward moving disturbances after noon during orthospiral IMF orientation. Causes suggested for TCVs originating at the magnetopause or in the low-latitude boundary layer include step-like changes in the dynamic pressure [*Kivelson and Southwood*, 1991], changes in the magnetopause reconnection rate [*Ridley et al.*, 1998], and Kelvin-Helmholtz instability [*McHenry et al.*, 1990]. The results of *Yahnin and Moretto* [1996], on the other hand, indicate that at least some TCVs may originate in the plasma sheet rather than at the magnetopause or in the low-latitude boundary layer.

Juusola et al. [2015] have examined how the extreme values of $|d\mathbf{J}_{eq}/dt|$ depend on season. In the present study, we have not accounted for different seasons. Nevertheless, ionospheric field-aligned current density and full horizontal as well as equivalent current density all depend on season [e.g., *Stauning*, 2002; *Juusola et al.*, 2014b]. Not taking the seasonal effect into account can lead to increased scatter in the results. Examining how $< |d\mathbf{J}_{eq}/dt| >$ depends on season remains a topic for a future study.

5. Conclusions

In this study, we have analyzed the behavior of the average time derivative of the ionospheric equivalent current vector ($< |d\mathbf{J}_{eq}/dt| >$) in the AACGM latitude range 54°–76°, derived from ground magnetic field data from the North European IMAGE magnetometer network for the 20 year period 1994–2013. Our main conclusions are the following:

1. In accordance with earlier studies [*Weigel et al.*, 2003], we found that $< |d\mathbf{J}_{eq}/dt| >$ as a function of latitude and MLT has two peaks: one in the premidnight sector and one in the prenoon sector. We found that the peaks are located at the nightside and dayside ends of the average westward electrojet, respectively.
2. The prenoon $< |d\mathbf{J}_{eq}/dt| >$ peak is most intense during fast solar wind speed and radial IMF orientation. Substorm activity does not significantly affect the prenoon peak.
3. The location of the prenoon $< |d\mathbf{J}_{eq}/dt| >$ peak is not significantly affected by the IMF orientation but persists at 8–10 MLT and 70°–75° latitude, near the boundary between the westward and eastward electrojets. Sensitivity of this boundary to disturbances is suggested as a possible explanation for the persistent prenoon location of the $< |d\mathbf{J}_{eq}/dt| >$ peak.
4. In accordance with earlier studies [e.g., *Fairfield and Cahill*, 1966], the premidnight $< |d\mathbf{J}_{eq}/dt| >$ peak is most intense during southward IMF orientation. We found that while faster solar wind speed mainly results in more intense activity in the premidnight sector, stronger IMF causes the intensified activity to spread to the postmidnight, dawn, and dusk sectors.
5. A good correspondence was found between development of the premidnight $< |d\mathbf{J}_{eq}/dt| >$ peak and average substorm bulge aurora and oval aurora as determined by *Gjerloev et al.* [2007]. The bulge aurora covers the western end of the westward electrojet where the equivalent current also has a significant poleward component. The oval aurora extends eastward along the purely westward electrojet.
6. The prenoon $< |d\mathbf{J}_{eq}/dt| >$ peak (maximum 0.58 A/km s) is on average more intense than the premidnight peak (maximum 0.50 A/km s), but according to *Juusola et al.* [2015], the most intense values of $< |d\mathbf{J}_{eq}/dt| >$ tend to occur in the premidnight and dawn sectors. These results indicate that as opposed to the premidnight peak, the prenoon peak results from relatively frequently occurring low-amplitude disturbances. IMF orientation affects the relative intensities of the two peaks: for IMF $B_z < 0$, the premidnight peak is stronger, and for radial IMF, the dayside peak.

Studies by *Schrijver and Mitchell* [2013] and *Schrijver et al.* [2014] show that there is a statistically significant increase in the number of insurance claims for the United States industrial electrical and electronic equipment during geomagnetically active days as characterized with enhanced dB/dt activity. These studies suggest that problems are not only associated with extreme events but persistent moderate forcing can cause an extra load for power grid infrastructure as well. Substorm activity in the midnight sector, driven by solar wind with IMF $B_z < 0$, is known to cause both extreme and moderate activities. Our study shows that power grids at high latitudes could be exposed to stress also in the prenoon sector, especially when solar wind speed is high and IMF is radial. The postnoon sector around ~16 MLT, on the other hand, should be quiet.

Acknowledgments
The IMAGE magnetometer data used in this paper are available at http://www.space.fmi.fi/image. The solar wind data used in this paper were extracted from NASA/GSFC's OMNI data set through the OMNIWeb interface http://omniweb.gsfc.nasa.gov/. The *AL* index data are available at http://wdc.kugi.kyoto-u.ac.jp/. We acknowledge the financial support by the Academy of Finland to the ReSoLVE Center of Excellence (project 272157). The research leading to these results has received funding from the European Union Seventh Framework Programme (FP7/2007-2013) under grant agreements 263325 (ECLAT) and 260330 (EURISGIC). We thank the institutes who maintain the IMAGE Magnetometer Array and acknowledge NASA/GSFC's Space Physics Data Facility's OMNIWeb service and OMNI data.

Michael Liehmohn thanks two anonymous reviewers for their assistance in evaluating this paper.

References

Akasofu, S.-I. (1964), The development of the auroral substorm, *Planet. Space Sci.*, *12*, 273–282.
Amm, O. (1997), Ionospheric elementary current systems in spherical coordinates and their application, *J. Geomagn. Geoelec.*, *49*, 947–955.

Amm, O., and A. Viljanen (1999), Ionospheric disturbance magnetic field continuation from the ground to ionosphere using spherical elementary current systems, *Earth Planets Space*, *51*, 431–440.

Anderson, B. J. (1994), An overview of spacecraft observations of 10 s to 600 s period magnetic pulsations in the Earth's magnetosphere, in *Solar Wind Sources of Magnetospheric Ultra-Low-Frequency Waves*, edited by M. J. Engebretson, K. Takahashi, and M. Scholer, pp. 25–43, AGU, Washington, D. C., doi:10.1029/GM081p0025

Andréeová, K., L. Juusola, E. K. J. Kilpua, and H. E. J. Koskinen (2014), Analysis of double-step response to an interplanetary shock in the dayside magnetosphere, *Ann. Geophys.*, *32*(10), 1293–1302, doi:10.5194/angeo-32-1293-2014.

Axford, W. I., and C. O. Hines (1961), A unifying theory of high-latitude geophysical phenomena and geomagnetic storms, *Can. J. Phys.*, *39*, 1433–1464.

Baker, K. B., and S. Wing (1989), A new magnetic coordinate system for conjugate studies at high latitudes, *J. Geophys. Res.*, *94*(A7), 9139–9143, doi:10.1029/JA094iA07p09139.

Birn, J., R. Nakamura, E. V. Panov, and M. Hesse (2011), Bursty bulk flows and dipolarization in MHD simulations of magnetotail reconnection, *J. Geophys. Res.*, *116*, A01210, doi:10.1029/2010JA016083.

Boteler, D. H., R. J. Pirjola, and H. Nevanlinna (1998), The effects of geomagnetic disturbances on electrical systems at the Earth's surface, *Adv. Space Res.*, *22*, 17–27, doi:10.1016/S0273-1177(97)01096-X.

Caan, M. N., R. L. McPherron, and C. T. Russell (1978), The statistical magnetic signature of magnetospheric substorms, *Planet. Space Sci.*, *26*(3), 269–279, doi:10.1016/0032-0633(78)90092-2.

Chen, C. X., and R. A. Wolf (1999), Theory of thin-filament motion in Earth's magnetotail and its application to bursty bulk flows, *J. Geophys. Res.*, *104*, 14,613–14,626.

Dungey, J. W. (1961), Interplanetary magnetic field and the auroral zones, *Phys. Rev. Lett.*, *6*, 47–48.

Dungey, J. W. (1963), The structure of the ionosphere, or adventures in velocity space, in *Geophysics: The Earth's Environment*, edited by C. DeWitt, J. Hiebolt, and A. Lebeau, pp. 526–536, Gordon and Breach, New York.

Eastwood, J. P., E. A. Lucek, C. Mazelle, K. Meziane, Y. Narita, J. Pickett, and R. A. Treumann (2005), The foreshock, *Space Sci. Rev.*, *118*(1–4), 41–94, doi:10.1007/s11214-005-3824-3.

Fairfield, D. H., and L. J. Cahill Jr. (1966), Transition region magnetic field and polar magnetic disturbances, *J. Geophys. Res.*, *71*(1), 155–169, doi:10.1029/JZ071i001p00155.

Finch, I. D., M. L. Lockwood, and A. P. Rouillard (2008), Effects of solar wind magnetosphere coupling recorded at different geomagnetic latitudes: Separation of directly-driven and storage/release systems, *Geophys. Res. Lett.*, *35*, L21105, doi:10.1029/2008GL035399.

Gjerloev, J. W., R. A. Hoffman, J. B. Sigwarth, and L. A. Frank (2007), Statistical description of the bulge-type auroral substorm in the far ultraviolet, *J. Geophys. Res.*, *112*, A07213, doi:10.1029/2006JA012189.

Gjerloev, J. W., R. A. Hoffman, J. B. Sigwarth, L. A. Frank, and J. B. H. Baker (2008), Typical auroral substorm: A bifurcated oval, *J. Geophys. Res.*, *113*, A03211, doi:10.1029/2007JA012431.

Guo, J., H. Liu, X. Feng, T. I. Pulkkinen, E. I. Tanskanen, C. Liu, D. Zhong, and Y. Wang (2014a), MLT and seasonal dependence of auroral electrojets: IMAGE magnetometer network observations, *J. Geophys. Res. Space Physics*, *119*, 3179–3188, doi:10.1002/2014JA019843.

Guo, J., T. I. Pulkkinen, E. I. Tanskanen, X. Feng, B. A. Emery, H. Liu, C. Liu, and D. Zhong (2014b), Annual variations in westward auroral electrojet and substorm occurrence rate during solar cycle 23, *J. Geophys. Res. Space Physics*, *119*, 2061–2068, doi:10.1002/2013JA019742.

Imber, S. M., S. E. Milan, and B. Hubert (2006), The auroral and ionospheric flow signatures of dual lobe reconnection, *Ann. Geophys.*, *24*, 3115–3129, doi:10.5194/angeo-24-3115-2006.

Imber, S. M., S. E. Milan, and B. Hubert (2007), Observations of significant flux closure by dual lobe reconnection, *Ann. Geophys.*, *25*, 1617–1627, doi:10.5194/angeo-25-1617-2007.

Juusola, L., N. Østgaard, E. Tanskanen, N. Partamies, and K. Snekvik (2011), Earthward plasma sheet flows during substorm phases, *J. Geophys. Res.*, *116*, A10228, doi:10.1029/2011JA016852.

Juusola, L., M. Kubyshkina, R. Nakamura, T. Pitkänen, O. Amm, K. Kauristie, N. Partamies, H. Rème, K. Snekvik, and D. Whiter (2013), Ionospheric signatures of a plasma sheet rebound flow during a substorm onset, *J. Geophys. Res. Space Physics*, *118*, 350–363, doi:10.1029/2012JA018132.

Juusola, L., S. E. Milan, M. Lester, A. Grocott, and S. Imber (2014a), Interplanetary magnetic field control of the ionospheric field-aligned current and convection distributions, *J. Geophys. Res. Space Physics*, *119*, 3130–3149, doi:10.1029/2013JA019455.

Juusola, L., et al. (2014b), Statistical comparison of seasonal variations in the GUMICS-4 global MHD model ionosphere and measurements, *Space Weather*, *11*, 582–600, doi:10.1002/2014SW001082.

Juusola, L., A. Viljanen, M. van de Kamp, E. I. Tanskanen, H. Vanhamäki, N. Partamies, and K. Kauristie (2015), High-latitude ionospheric equivalent currents during strong space storms: Regional perspective, *Space Weather*, *13*, 49–60, doi:10.1002/2014SW001139.

Kamide, Y., P. D. Perreault, S.-I. Akasofu, and J. D. Winningham (1977), Dependence of substorm occurrence probability on the interplanetary magnetic field and on the size of the auroral oval, *J. Geophys. Res.*, *82*(35), 5521–5528.

Kivelson, M., and D. Southwood (1991), Ionospheric traveling vortex generation by solar wind buffeting of the magnetosphere, *J. Geophys. Res.*, *96*(A2), 1661–1667.

Korotova, G. I., D. G. Sibeck, H. J. Singer, T. J. Rosenberg, and M. J. Engebretson (2004), Interplanetary magnetic field control of dayside transient event occurrence and motion in the ionosphere and magnetosphere, *Ann. Geophys.*, *22*(12), 4197–4202, doi:10.5194/angeo-22-4197-2004.

Lanzerotti, L. J., R. M. Konik, A. Wolfe, D. Venkatesan, and C. G. Maclennan (1991), Cusp latitude magnetic impulse events: 1. Occurrence statistics, *J. Geophys. Res.*, *96*(A8), 14,009–14,022, doi:10.1029/91JA00567.

Lockwood, M., L. Barnard, H. Nevanlinna, M. J. Owens, R. G. Harrison, A. P. Rouillard, and C. J. Davis (2013a), Reconstruction of geomagnetic activity and near-Earth interplanetary conditions over the past 167 yr—Part 1: A new geomagnetic data composite, *Ann. Geophys.*, *31*(11), 1957–1977, doi:10.5194/angeo-31-1957-2013.

Lockwood, M., L. Barnard, H. Nevanlinna, M. J. Owens, R. G. Harrison, A. P. Rouillard, and C. J. Davis (2013b), Reconstruction of geomagnetic activity and near-Earth interplanetary conditions over the past 167 yr—Part 2: A new reconstruction of the interplanetary magnetic field, *Ann. Geophys.*, *31*(11), 1979–1992, doi:10.5194/angeo-31-1979-2013.

Lockwood, M., H. Nevanlinna, M. Vokhmyanin, D. Ponyavin, S. Sokolov, L. Barnard, M. J. Owens, R. G. Harrison, A. P. Rouillard, and C. J. Scott (2014a), Reconstruction of geomagnetic activity and near-Earth interplanetary conditions over the past 167 yr—Part 3: Improved representation of solar cycle 11, *Ann. Geophys.*, *32*(4), 367–381, doi:10.5194/angeo-32-367-2014.

Lockwood, M., H. Nevanlinna, L. Barnard, M. J. Owens, R. G. Harrison, A. P. Rouillard, and C. J. Scott (2014b), Reconstruction of geomagnetic activity and near-Earth interplanetary conditions over the past 167 yr—Part 4: Near-Earth solar wind speed, IMF, and open solar flux, *Ann. Geophys.*, *32*(4), 383–399, doi:10.5194/angeo-32-383-2014.

Lotko, W., R. H. Smith, B. Zhang, J. E. Ouellette, O. J. Brambles, and J. G. Lyon (2014), Ionospheric control of magnetotail reconnection, *Science*, *345*(6193), 184–187, doi:10.1126/science.1252907.

Luhmann, J. G., R. J. Walker, C. T. Russell, N. U. Crooker, J. R. Spreiter, and S. S. Stahara (1984), Patterns of potential magnetic field merging sites on the dayside magnetopause, *J. Geophys. Res.*, *89*(A3), 1739–1742.

Marsch, E., and C.-Y. Tu (1990), On the radial evolution of MHD turbulence in the inner heliosphere, *J. Geophys. Res.*, *95*(A6), 8211–8229, doi:10.1029/JA095iA06p08211.

McHenry, M. A., C. R. Clauer, E. Friis-Christensen, P. T. Newell, and J. D. Kelly (1990), Ground observations of magnetospheric boundary layer phenomena, *J. Geophys. Res.*, *95*(A9), 14,995–15,005, doi:10.1029/JA095iA09p14995.

McPherron, R. L., T.-S. Hsu, J. Kissinger, X. Chu, and V. Angelopoulos (2011), Characteristics of plasma flows at the inner edge of the plasma sheet, *J. Geophys. Res.*, *116*, A00I33, doi:10.1029/2010JA015923.

Milan, S. E. (2004), Dayside and nightside contributions to the cross polar cap potential: Placing an upper limit on a viscous-like interaction, *Ann. Geophys.*, *22*, 3771–3777, doi:10.5194/angeo-22-3771-2004.

Milan, S. E., T. A. Evans, and B. Hubert (2010), Average auroral configuration parameterized by geomagnetic activity and solar wind conditions, *Ann. Geophys.*, *28*(4), 1003–1012, doi:10.5194/angeo-28-1003-2010.

Nakamura, R., et al. (2013), Flow bouncing and electron injection observed by Cluster, *J. Geophys. Res. Space Physics*, *118*, 2055–2072, doi:10.1002/jgra.50134.

Newell, P. T., T. Sotirelis, K. Liou, C. -I. Meng, and F. J. Rich (2007), A nearly universal solar wind-magnetosphere coupling function inferred from 10 magnetospheric state variables, *J. Geophys. Res.*, *112*, A01206, doi:10.1029/2006JA012015.

Ohtani, S., Y. Miyashita, H. Singer, and T. Mukai (2009), Tailward flows with positive B_Z in the near-Earth plasma sheet, *J. Geophys. Res.*, *114*, A06218, doi:10.1029/2009JA014159.

Panov, E. V., et al. (2010a), Multiple overshoot and rebound of a bursty bulk flow, *Geophys. Res. Lett.*, *37*, L08103, doi:10.1029/2009GL041971.

Panov, E. V., et al. (2010b), Plasma sheet thickness during a bursty bulk flow reversal, *J. Geophys. Res.*, *115*, A05213, doi:10.1029/2009JA014743.

Partamies, N., L. Juusola, E. Tanskanen, and K. Kauristie (2013), Statistical properties of substorms during different storm and solar cycle phases, *Ann. Geophys.*, *31*, 349–358, doi:10.5194/angeo-31-349-2013.

Pirjola, R. (2000), Geomagnetically induced currents during magnetic storms, *IEEE Trans. Plasma Sci.*, *28*, 1867–1873, doi:10.1109/27.902215.

Ridley, A. J., T. Moretto, P. Ernström, and C. R. Clauer (1998), Global analysis of three traveling vortex events during the November 1993 storm using the assimilative mapping of ionospheric electrodynamics technique, *J. Geophys. Res.*, *103*(A11), 26,349–26,358, doi:10.1029/97JA03433.

Roe, P. L. (1981), Approximate Riemann solvers, parameter vectors, and difference schemes, *J. Comput. Phys.*, *43*(2), 357–372, doi:10.1016/0021-9991(81)90128-5.

Russell, C. T. (1972), The configuration of the magnetosphere, in *Critical Problems of Magnetospheric Physics*, edited by E. R. Dyer, pp. 1–16, IUCSTP Secretariat, Washington, D. C.

Schrijver, C. J., and S. D. Mitchell (2013), Disturbances in the US electric grid associated with geomagnetic activity, *J. Space Weather Space Clim.*, *3*, A19, doi:10.1051/swsc/2013041.

Schrijver, C. J., R. Dobbins, W. Murtagh, and S. M. Petrinec (2014), Assessing the impact of space weather on the electric power grid based on insurance claims for industrial electrical equipment, *Space Weather*, *12*, 487–498, doi:10.1002/2014SW001066.

Shiokawa, K., W. Baumjohann, and G. Haerendel (1997), Braking of high-speed flows in the near-Earth tail, *Geophys. Res. Lett.*, *24*(10), 1179–1182.

Snekvik, K., E. I. Tanskanen, and E. K. J. Kilpua (2013), An automated identification method for Alfvénic streams and their geoeffectiveness, *J. Geophys. Res. Space Physics*, *118*, 5986–5998, doi:10.1002/jgra.50588.

Stauning, P. (2002), Field-aligned ionospheric current systems observed from Magsat and Oersted satellites during northward IMF, *Geophys. Res. Lett.*, *29*(15), 8005, doi:10.1029/2001GL013961.

Tanskanen, E. I. (2009), A comprehensive high-throughput analysis of substorms observed by IMAGE magnetometer network: Years 1993–2003 examined, *J. Geophys. Res.*, *114*, A05204, doi:10.1029/2008JA013682.

Tanskanen, E. I., A. Viljanen, T. I. Pulkkinen, R. Pirjola, L. Häkkinen, A. Pulkkinen, and O. Amm (2001), At substorm onset, 40% of AL comes from underground, *J. Geophys. Res.*, *106*, 13,119–13,134.

Tanskanen, E. I., T. I. Pulkkinen, A. Viljanen, K. Mursula, N. Partamies, and J. A. Slavin (2011), From space weather toward space climate time scales: Substorm analysis from 1993 to 2008, *J. Geophys. Res.*, *116*, A00I34, doi:10.1029/2010JA015788.

Vanhamäki, H., and O. Amm (2011), Analysis of ionospheric electrodynamic parameters on mesoscales—A review of selected techniques using data from ground-based observation networks and satellites, *Ann. Geophys.*, *29*(3), 467–491, doi:10.5194/angeo-29-467-2011.

Viljanen, A. (1997), The relation between geomagnetic variations and their time derivatives and implications for estimation of induction risks, *Geophys. Res. Lett.*, *24*(6), 631–634, doi:10.1029/97GL005380.

Viljanen, A., and E. Tanskanen (2011), Climatology of rapid geomagnetic variations at high latitudes over two solar cycles, *Ann. Geophys.*, *29*(10), 1783–1792, doi:10.5194/angeo-29-1783-2011.

Viljanen, A., H. Nevanlinna, K. Pajunpää, and A. Pulkkinen (2001), Time derivative of the horizontal geomagnetic field as an activity indicator, *Ann. Geophys.*, *19*(9), 1107–1118, doi:10.5194/angeo-19-1107-2001.

Viljanen, A., E. I. Tanskanen, and A. Pulkkinen (2006), Relation between substorm characteristics and rapid temporal variations of the ground magnetic field, *Ann. Geophys.*, *24*(2), 725–733, doi:10.5194/angeo-24-725-2006.

van de Kamp, M. (2013), Harmonic quiet-day curves as magnetometer baselines for ionospheric current analyses, *Geosci. Instrum. Method Data Syst.*, *2*, 289–304, doi:10.5194/gi-2-289-2013.

Weigel, R. S., A. J. Klimas, and D. Vassiliadis (2003), Solar wind coupling to and predictability of ground magnetic fields and their time derivatives, *J. Geophys. Res.*, *1298*(A7), doi:10.1029/2002JA009627.

Weimer, D. R. (1995), Models of high-latitude electric potentials derived with a least error fit of spherical harmonic coefficients, *J. Geophys. Res.*, *100*(A10), 19,595–19,607, doi:10.1029/95JA01755.

Weimer, D. R. (1996), A flexible, IMF dependent model of high-latitude electric potentials having "space weather" applications, *Geophys. Res. Lett.*, *23*(18), 2549–2552.

Weimer, D. R., D. M. Ober, N. C. Maynard, M. R. Collier, D. J. McComas, N. F. Ness, C. W. Smith, and J. Watermann (2003), Predicting interplanetary magnetic field (IMF) propagation delay times using the minimum variance technique, *J. Geophys. Res.*, *1026*(A1), doi:10.1029/2002JA009405.

Weygand, J. M., O. Amm, V. Angelopoulos, S. E. Milan, A. Grocott, H. Gleisner, and C. Stolle (2012), Comparison between SuperDARN flow vectors and equivalent ionospheric currents from ground magnetometer arrays, *J. Geophys. Res.*, *117*, A05325, doi:10.1029/2011JA017407.

Wing, S., S. Ohtani, P. T. Newell, T. Higuchi, G. Ueno, and J. M. Weygand (2010), Dayside field-aligned current source regions, *J. Geophys. Res.*, *115*, A12215, doi:10.1029/2010JA015837.

Yahnin, A., and T. Moretto (1996), Travelling convection vortices in the ionosphere map to the central plasma sheet, *Ann. Geophys.*, *14*, 1025–1031, doi:10.1007/s00585-996-1025-3.